

SYNTHESIS AND CHARACTERIZATION OF IRON-COPPER NITRIDE
THIN FILMS

BY

HRISHIKESH KAMAT

A THESIS
SUBMITTED TO THE FACULTY OF

ALFRED UNIVERSITY

IN PARTIAL FULFILLMENT OF THE REQUIREMENTS
FOR THE DEGREE OF

MASTER OF SCIENCE

IN

MATERIALS SCIENCE AND ENGINEERING

ALFRED, NEW YORK

SEPTEMBER, 2016

Alfred University theses are copyright protected and may be used for education or personal research only. Reproduction or distribution in part or whole is prohibited without written permission from the author.

Signature page may be viewed at Scholes Library, New York State College of Ceramics, Alfred University, Alfred, New York.

SYNTHESIS AND CHARACTERIZATION OF IRON-COPPER NITRIDE
THIN FILMS

BY

HRISHIKESH KAMAT

B.S. NATIONAL INSTITUTE OF TECHNOLOGY, SRINAGAR (2011)

SIGNATURE OF AUTHOR _____

APPROVED BY _____

XINGWU WANG, ADVISOR

STEVEN M. PILGRIM, ADVISORY COMMITTEE

WILLIAM C. LACOURSE, ADVISORY COMMITTEE

CHAIR, ORAL THESIS DEFENSE

ACCEPTED BY _____

ALASTAIR N. CORMACK, INTERIM DEAN
KAZUO INAMORI SCHOOL OF ENGINEERING

ACKNOWLEDGMENTS

I would like to thank Dr. Xingwu Wang for the guidance and encouragement he provided during my graduate research and for financially supporting me during my graduate studies. I would also like to thank my thesis committee members; Dr. Steven M. Pilgrim and Dr. William C. LaCourse for providing me valuable feedback on my written thesis. A special thanks to Dr. Steven Tidrow for supporting me financially and encouraging me with his positive words. I would like to extend my gratitude to Dr. Hao Zeng, James Parry, Dr. Yueling Qin and Dr. Ruikun Pan at the University of Buffalo for helping me with Sputter deposition of my thin films and FIB analysis. I also wish to thank Ms. Rosalie DiRaimondo, Mr. Swavek Zdzieszynski, Mr. Gerald Wynick, Mr. James Theibaud and Mr. Ding Ding for their help. Finally, I would like to thank my parents and family who have stood resolutely behind me during my good and bad times. I also take this opportunity to thank my fiancée Dimple Pradhan for her unconditional love and support and for bringing stability in my life during these times of turmoil.

This work made use of the Cornell Center for Materials Research Shared Facilities which are supported through the NSF MRSEC program (DMR-1120296). It was partially supported by NSF DMR-1229208 and SUNY RF4E.

Table of Contents

	Page
Acknowledgments	iii
List of Tables	v
List of Figures	vii
Abstract	xi
I. INTRODUCTION.....	1
A. Background and Motivation	1
B. Literature Review	2
II. EXPERIMENTAL PROCEDURE.....	5
A. Thin film deposition	5
B. X-ray Diffraction	7
C. Scanning Electron Microscopy and Energy Dispersive X-Ray Spectroscopy	7
D. X-ray Photoelectron Spectroscopy	8
E. X-ray Reflectivity	8
F. Magnetic Measurements.....	9
III. RESULTS AND DISCUSSION.....	10
A. Thin Film Processing.....	10
B. X-ray Diffraction	10
C. Scanning Electron Microscopy and Energy Dispersive X-ray Spectroscopy.....	16
D. X-ray Photoelectron Spectroscopy	29
E. X-Ray Reflectivity.....	44
F. Vibrational Sample Magnetometry.....	51
IV. CONCLUSION.....	59
REFERENCES.....	60
APPENDIX.....	65

LIST OF TABLES

	Page
Table I. Fabrication conditions for thin film samples.	10
Table II. X-ray diffraction parameters of samples A, B, C and D.....	12
Table III. X-ray diffraction parameters for samples E, F, G and H.....	14
Table IV. X-ray diffraction parameters for samples J and K.....	15
Table V. Thicknesses of thin film samples as measured from cross-sectional SEM images.	22
Table VI. Relative atomic ratio of copper in the iron-copper nitride films.	28
Table VII. Deconvoluted peak parameters for the Fe 2p region of samples A, B, C and D.	35
Table VIII. Deconvoluted peak parameters for the Fe 2p region of samples E, F, G and H.	38
Table IX. Binding energy values of the Cu 2p region of samples F, G and H.	41
Table X. Binding energy values for the Fe 2p region of samples J and K.	43
Table XI. Binding energy values for the Cu 2p region of samples J and K.....	44
Table XII. XRR curve fitting parameters for samples A, B, C and D.....	47
Table XIII.XRR curve fitting parameters for samples E, F, G and H.	50
Table XIV.XRR curve fitting parameters for sample J and K.....	51
Table XV. Magnetic parameters for samples A, B, C and D extracted from their VSM curves.	53
Table XVI.Magnetic parameters for samples E, F, G and H extracted from the VSM curves.	56

Table XVII. Magnetic parameters for samples J and K extracted from the VSM curves. 57

LIST OF FIGURES

	Page
Figure 1. Schematic representation of the sputter deposition chamber.	6
Figure 2. Stacked x-ray diffraction patterns for sample A, B, C and D.	11
Figure 3. Stacked x-ray diffraction patterns of samples E, F, G and H.....	13
Figure 4. Stacked x-ray diffraction patterns of samples J and K.....	15
Figure 5. Representative SEM surface micrograph of sample A (scale bar - 100 nm)..	16
Figure 6. Representative SEM surface micrograph of sample B (scale bar - 100 nm)..	17
Figure 7. Representative SEM surface micrograph of sample C (scale bar - 100 nm)..	17
Figure 8. Representative SEM surface micrograph of sample D (scale bar - 100 nm)..	18
Figure 9. Representative SEM surface micrograph of sample E (scale bar - 100 nm)..	19
Figure 10. Representative SEM surface micrograph of sample F (scale bar - 100 nm)..	19
Figure 11. Representative SEM surface micrograph of sample G (scale bar - 100 nm)..	20
Figure 12. Representative SEM surface micrograph of sample H (scale bar - 100 nm)..	20
Figure 13. Representative SEM surface micrograph of sample J (scale bar - 100nm)..	21
Figure 14. Representative SEM surface micrograph of sample K (scale bar - 100 nm)..	21
Figure 15. Cross-sectional SEM micrograph of sample A (scale bar - 100 nm).	23
Figure 16. Cross-sectional SEM micrograph of sample B (scale bar - 100 nm).....	23
Figure 17. Cross-sectional SEM micrograph of sample C (scale bar – 100 nm).	24
Figure 18. Cross-sectional SEM micrograph of sample D (scale bar - 100 nm).	24

Figure 19. Cross-sectional SEM micrograph of sample E (scale bar - 100 nm).....	25
Figure 20. Cross-sectional SEM micrograph of sample F (scale bar - 100 nm).....	25
Figure 21. Cross-sectional SEM micrograph of sample G (scale bar - 100 nm).	26
Figure 22. Cross-sectional SEM micrograph of sample H (scale bar - 100 nm).	26
Figure 23. Cross-sectional SEM micrograph of sample J (scale bar - 100 nm).....	27
Figure 24. Cross-sectional SEM micrograph of sample K (scale bar - 100 nm).	27
Figure 25. High resolution XPS spectrum for the Fe 2p region of the iron sputtering target after Ar ⁺ sputtering to remove contaminants.....	29
Figure 26. High resolution XPS spectrum for the Cu 2p region of the iron sputtering target after Ar ⁺ sputtering to remove contaminants.	30
Figure 27. XPS survey spectra for samples A, B, C and D.....	31
Figure 28. XPS survey spectra for samples E, F, G and H.	31
Figure 29. XPS survey spectra for samples J and K.	32
Figure 30. High resolution XPS spectrum for the Fe 2p region of sample A.	33
Figure 31. High resolution XPS spectrum for the Fe 2p region of sample B.	34
Figure 32. High resolution XPS spectrum for the Fe 2p region of sample C.	34
Figure 33. High resolution XPS spectrum for the Fe 2p region of sample D.	35
Figure 34. High resolution XPS spectrum for the Fe 2p region of sample E.....	36
Figure 35. High resolution XPS spectrum for the Fe 2p region of sample F.....	37
Figure 36. High resolution XPS spectrum for the Fe 2p region of sample G.	37
Figure 37. High resolution XPS spectrum for the Fe 2p region of sample H.	38
Figure 38. High resolution XPS spectrum for the Cu 2p region of sample F.	39

Figure 39. High resolution XPS spectrum for the Cu 2p region of sample G.....	40
Figure 40. High resolution XPS spectrum for the Cu 2p region of sample H.....	40
Figure 41. High resolution XPS spectrum for the Fe 2p region of sample J.	42
Figure 42. High resolution XPS spectrum for the Fe 2p region of sample K.	42
Figure 43. High resolution XPS spectrum for the Cu 2p region of sample J.....	43
Figure 44. High resolution XPS spectrum for the Cu 2p region of sample K.....	44
Figure 45. Raw (measured) and simulated XRR curves of samples A, B, C and D. Raw (Black), Simulated (Blue).	46
Figure 46. Thickness comparison of samples A, B, C and D predicted from XRR curve fitting (total thickness - all three layers) and cross-sectional SEM measurements.....	47
Figure 47. Raw (measured) and simulated XRR curves of samples E, F, G and H. Raw (Black), Simulated (Blue).	49
Figure 48. Thickness comparison of samples E, F, G and H predicted from XRR curve fitting of three layers and cross-sectional SEM measurement.....	50
Figure 49. Hysteresis curves for samples A, B, C and D.....	52
Figure 50. Expanded hysteresis curves for samples A, B, C and D.	53
Figure 51. Hysteresis curve for samples E, F, G and H.....	55
Figure 52. Expanded hysteresis curves for samples E, F, G and H.	55
Figure 53. Hysteresis curves of samples J and K.....	56
Figure 54. Expanded hysteresis curve for samples J and K.....	57
Figure 55. FIB micrograph of sample D fabricated at nitrogen flow rate of 5 sccm.....	65
Figure 56. FIB micrograph of sample E fabricated at nitrogen flow rate of 5 sccm and a copper sputtering power of 10 W.....	65

Figure 57. FIB micrograph of sample F fabricated at nitrogen flow rate of 5 sccm and a copper sputtering of 20 W..... 66

Figure 58. FIB micrograph of sample G fabricated at nitrogen flow rate of 5 sccm and a copper sputtering of 30 W..... 66

Figure 59. FIB micrograph of sample H fabricated at nitrogen flow rate of 5 sccm and a copper sputtering of 40 W..... 67

ABSTRACT

In the present work, thin films of iron nitride and iron-copper nitride have been fabricated on silicon substrates by reactive magnetron sputtering. The experimental conditions such as reactive gas flow rate and power required to yield these films have been systematically varied. The structure, composition, and morphology of the as-fabricated films have been investigated by x-ray diffraction (XRD), x-ray photoelectron spectroscopy (XPS), energy dispersive x-ray spectroscopy (EDS), scanning electron microscopy (SEM) and x-ray reflectivity (XRR). The magnetic properties are characterized via vibrational sample magnetometry (VSM), and are found to be related to the structure, composition and morphology of the films. Results are discussed in terms of potential applications of these materials in magnetic applications.

I. INTRODUCTION

A. Background and Motivation

Thin film technology has rapidly advanced over the past few decades due to the need for new products and devices in the electronics and optical industries. A specific focus has been on magnetic thin films as there is an increasing and continuous demand for information and the means to store it in digital form¹. The area of thin-film magnetism lays emphasis on the concept that thin film materials behave differently from their bulk counterparts and that by controlling the various fabrication parameters for these films, the magnetic properties of these films can be tuned to suit specific applications.

Transition metal nitride thin films form one such interesting class of materials due to their versatile magnetic, electrical, mechanical and tribological properties²⁻⁶. The binary iron nitrides have received special attention due to their potential applications in magnetic sensors and storage devices⁷⁻⁹; in addition one iron nitride phase exhibits a giant magnetic moment¹⁰. Studies have suggested that doping tin, manganese, nickel, cobalt, aluminum, titanium, etc. to these binary iron nitrides helps tune the magnetic properties of these films for specific applications¹¹⁻¹⁸. Copper doped nitrides have been considered as suitable candidates for nitride based spin aligners in the past¹⁹. Layered thin film structures of iron nitride and copper nitride²⁰⁻²², and iron-copper nitrides in the bulk phase²³ have been found to tune the magnetic properties of the base iron nitride. However, there is no literature available on copper incorporated iron nitride thin films

Thus, the motivation behind this work was to study the effects of copper incorporation on the structure and magnetic properties of iron nitride thin films. Iron nitride thin films were initially fabricated at different nitrogen flow rates by reactive magnetron sputtering to establish the baseline parameters for copper addition. Then copper was systematically incorporated in these films by co-sputtering with iron to fabricate iron-copper nitride thin films. The influence of nitrogen flow rate and copper sputtering power on the structure, morphology and composition were then investigated using different characterization techniques. Magnetic measurements were conducted on

these films and an attempt was made to correlate the magnetic properties with the film fabrication conditions.

B. Literature Review

A study of different iron nitride phases was first conducted as early as 1950 by K. H. Jack whose work led to the development of the first iron-nitrogen phase diagram^{24,25}. The interest in the iron-nitrogen system was further enhanced by an observation of a giant magnetic moment for α'' -Fe₁₆N₂ phase by T. K. Kim and M. Takahashi in 1972¹⁰. It was observed that depending on the nitrogen content, iron nitride phases with different structures and magnetic properties could be formed. At very low nitrogen concentration, α -Fe was found to exist as a pure phase²⁶. It is ferromagnetic with a saturation magnetization value of 1714 emu/cm³ (1.714×10⁶ A/m, 1 emu/cm³ = 10³ A/m) reported in literature²⁷. Upon increasing the nitrogen content slightly, γ -Fe phase which is non-magnetic was found to co-exist with α -Fe²⁸. The α' -Fe₈N phase was formed when the γ -Fe phase was rapidly quenched^{26,29}. In this phase, the nitrogen atoms occupy a random octahedral site in the Fe sub lattice. The α' -Fe₈N phase transforms into α'' -Fe₁₆N₂ phase upon annealing which leads to the ordering of the nitrogen atoms²⁹. It possesses the highest saturation magnetization (2050 emu/cm³)³⁰ amongst all the iron nitride phases. Further increasing the nitrogen concentration, results in the formation of the γ' -Fe₄N phase which has a face centered cubic crystal structure with the nitrogen atom occupying the body centered cubic position²⁹. This phase exhibits ferromagnetic behavior with a saturation magnetization of 1442 emu/cm³ reported in literature³¹⁻³³. The γ' -Fe₄N exists as a pure phase within a very narrow range of nitrogen concentration and decomposes to (γ' -Fe₄N + α -Fe) on the iron rich side and to (γ' -Fe₄N + ϵ -Fe_xN) where 2 < x ≤ 3 on the nitrogen rich side^{1,25}. The ϵ -Fe_xN (2 < x ≤ 3) phase has a saturation magnetization value lower than that of γ' -Fe₄N. Increasing the nitrogen concentration the iron nitride converts to ζ -Fe₂N phase which is also found to be a non-magnetic phase.

Various thin film deposition techniques have been used to deposit these iron nitride thin films. Sputter deposition has been widely used due to its universality, ability to control compositions and to form iron nitride phases which are difficult to prepare by common chemical methods³⁴. Lo et al.³⁵ demonstrated that iron nitride thin films could

be fabricated by reactive sputtering in a mixture of argon and nitrogen gases. Later, S. Wang and M. H. Kryder reported a study on iron nitride thin films fabricated by RF-diode sputtering⁸. The phase formation in their films depended on the ratio of nitrogen to argon flow rates; at a lower ratio, α -Fe was the dominant phase. Increasing the N₂: Ar rate ratios promoted the formation of γ' -Fe₄N. The saturation magnetization decreased with increasing flow rate ratio. Similar observations were reported by D. H. Mosca et al. for films fabricated by dc reactive magnetron sputtering³⁶. Their x-ray diffraction results suggested that on increasing the nitrogen partial pressure, the synthesized phase changed from an iron rich phase (α -Fe) to a nitrogen rich phase (ζ -Fe₂N). At an intermediate nitrogen partial pressure, a multiphase mixture of α -Fe, γ' -Fe₄N, ϵ -(Fe₂N-Fe₃N) and ζ -Fe₂N was formed in the film. The pure α -Fe film recorded the highest saturation magnetization values among all the films, decreasing with an increasing nitrogen partial pressure. The presence of paramagnetic ζ -Fe₂N phase resulted in the lowest saturation magnetization and absence of magnetic hysteresis (M vs. H loop) for the film fabricated at the highest nitrogen partial pressure. In a study by Gao et al.¹⁵, films containing multiple iron nitride phases (α -Fe, α'' -Fe₁₆N₂ and γ' -Fe₄N) were obtained by reactive magnetron sputtering. The volume fractions of each of these phases depended on the nitrogen to argon flow ratio and the films with a dominant α'' -Fe₁₆N₂ phase showed the highest saturation magnetization exceeding that of bulk iron.

Interstitial atoms play an important role in tuning the magnetic properties of the iron based compounds^{37,38}. Studies have shown that iron nitrides can be doped by replacing iron atoms in the Fe-N lattice by Group IIIA or transition metals without altering the crystal structure of the host nitrides. This was found to modify magnetic properties and control grain morphology which could be useful for specific applications. The host nitrides commonly doped were γ' -Fe₄N and ϵ -Fe₃N⁶. Studies conducted on doping of manganese confirmed that manganese substitutes both the corner and the face-centered iron atoms in the γ' -Fe₄N lattice¹². The substitution increased the remanence magnetization (M_r) over saturation magnetization (M_s) and decreased the grain size. Gao et al.,¹⁵ studied the effects of substituting cobalt and nickel in γ' -Fe₄N. They observed a decrease in the saturation magnetization (M_s) with increasing nickel concentration which was attributed to the increase in the number of 3d electrons and thus a reduced difference

between spin-up and spin-down 3d electrons. The magnetic studies of nickel substituted γ' -Fe₄N compounds by R.N. Panda and N.S. Gajbhiye confirmed that lattice constant and saturation magnetization for γ' -Fe_{4-x}Ni_xN decreased with increasing nickel concentration³. This decrease in the saturation magnetization was attributed to the presence of a canted spin structure and/or oxide layer formation at the surface. Adding tantalum to the FeN films reduced the grain size and inhibited the formation of the γ' -Fe₄N phase which was found to affect its magnetic properties³⁹. Theoretical studies conducted on the structure and magnetic properties of cobalt, chromium and titanium doped γ' -Fe₄N suggested that CoFe₃N is ferromagnetic, CrFe₃N is ferrimagnetic and TiFe₃N is a non-magnetic phase with no net magnetic moments⁴⁰. Gajbhiye et al. conducted studies on the substitution of cobalt and nickel in the ϵ -Fe₃N lattice. They found that cobalt substitution results in the formation of ϵ -Co_xFe_{3-x}N phase along with a bcc α -Fe phase and nickel substitution formed the γ' -Fe_{4-x}Ni_xN phase⁴¹. R. N. Panda et al. recently reported that with progressive substitution by Ni atoms, the ϵ -Fe₃N phase changed to γ' -Fe_{4-x}Ni_xN phase and the value of the saturation magnetization was found to increase with the increase in the nickel content to $x = 0.6$ and decreased thereafter¹⁸. Copper substitution in iron nitrides obtained by mechanical alloying has been found to form γ' -Cu_xFe_{4-x}N nitrides in which the magnetization decreases when iron atoms are substituted with copper atoms²³. Overall, literature provides examples of doping that alter the magnetic properties of iron nitrides.

In this thesis we addressed two main questions:

- Is it possible to fabricate iron-copper nitride thin films containing copper doped iron nitride phases?
- Is it possible to modify the magnetic properties of these thin films by controlling the copper concentration (sputtering powers)?

II. EXPERIMENTAL PROCEDURE

A. Thin film deposition

Thin films were deposited by reactive magnetron sputtering inside an AJA Inc. ATC UHV Dual Chamber Deposition System. The system is equipped with a load lock and a main deposition chamber. The load lock is maintained at a base pressure of 8×10^{-5} Pa prior to deposition to ensure that the system is kept under high vacuum, thus minimizing the presence of residual gas during deposition. Figure 1 shows the schematic diagram of the sputter deposition chamber. The chamber diameter is 25.4 cm (10 inches) and is equipped with a motorized substrate holder rotation facility and an IR substrate heater. The diameter of the substrate holder is 7.62 cm (3 inches).

High purity iron and copper sputter targets obtained from PRAM Inc. were used. Target diameters were 3.81 cm (1.5 inches) with thicknesses of 0.254 cm (0.1 inches) and 0.508 cm (0.2 inches) for the iron and copper targets respectively. The targets were placed inside the shuttered magnetron sputtering gun prior to deposition. The iron target was sputtered using a dc power source (A3DC) while the copper target was sputtered using an RF power source (R301) operating at a frequency of 13.56 MHz. Argon was flowed inside the deposition chamber onto the target, while nitrogen entered the deposition chamber near the substrate. The argon flow was fixed at 50 sccm while the nitrogen flow was changed from 0.6 sccm to 5.0 sccm for iron nitride films and from 1.2 sccm to 5.0 sccm for iron-copper nitride films. The thin films were deposited on a Si (100) phosphorous doped n-type wafer with a natively grown oxide layer on top. The thickness of the wafer ranges from 500 to 550 μm and the flatness is less than 5 μm . The substrate heater temperature was maintained at 300°C for the entire duration of the experiment for all the samples.

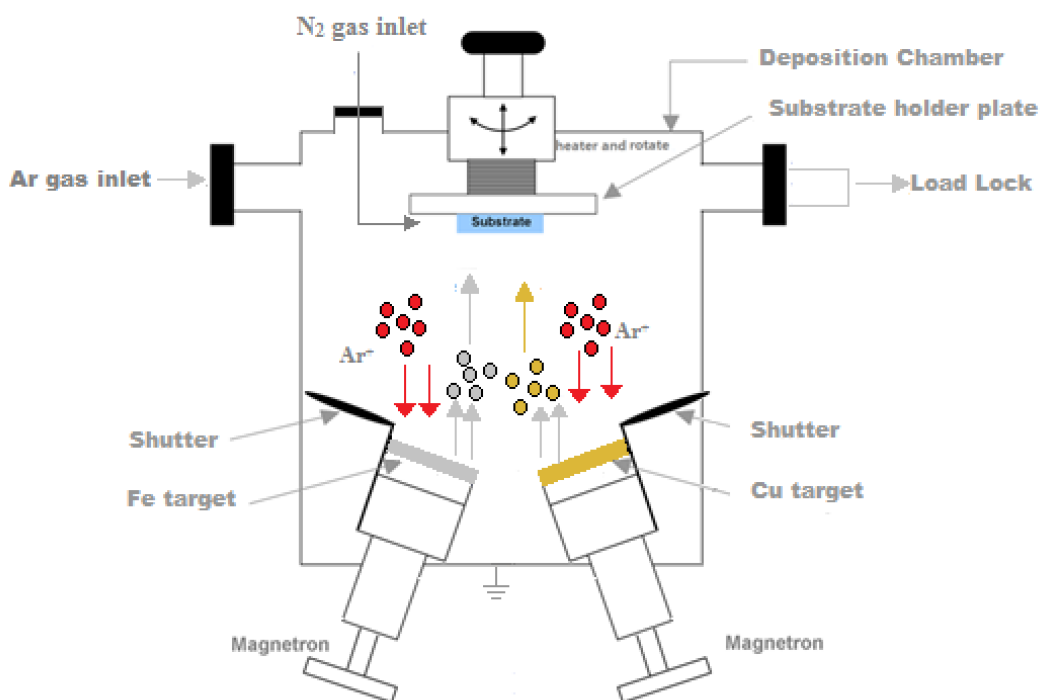


Figure 1. Schematic representation of the sputter deposition chamber.

The process for depositing co-sputtered films of iron and copper in the presence of nitrogen and argon followed this general procedure. The silicon substrate was mounted on an Inconel substrate holder and the surface was blown with nitrogen to dislodge any dust or particulates that had developed on the substrate during the mounting process. The substrate holder was then introduced face down inside the load lock, onto the transfer arm. The load lock was then pumped down for approximately twenty minutes and the substrate holder was then transferred to the deposition chamber. The transfer arm was then withdrawn; the gate valve closed, and the substrate holder and the heater assembly were lowered into place above the sputtering source. The distance between the sputtering source and the substrate holder (deposition height) was maintained at 25 cm. The rotation was then set to 30 rpm and the heater temperature was ramped up to 300°C. Argon was then flowed into the sputtering source at a rate of 50 sccm to a pressure of approximately 30 mTorr (3.947 Pa). The dc power supply connected to the shuttered magnetron sputtering gun holding the iron target was then turned on and the power was gradually ramped from 0 to 80 W. The voltage and current observed at a power of 80 W were 460

V and 180 mA respectively. Once the plasma was initiated, the pressure was reduced to 3 mTorr (0.395 Pa). Similarly, the 'RF' power supply connected to the shuttered magnetron sputtering gun holding the copper target was switched on and a copper power was set. The voltage varied from 150 to 210 V depending on the copper power (10 - 40 W). After sputtering both the targets at a low pressure for approximately two minutes, nitrogen was introduced into the system at the desired flow rate (5 sccm or 1.2 sccm). Once the nitrogen flow and the sputtering rates were stabilized (2 - 3 minutes), the shutters on top of the magnetron sputtering guns holding the iron and copper sputtering targets were opened to allow deposition of Fe-Cu-N onto the heated substrate. Once the film was deposited for the desired time, the shutters were then closed, the heater and the gases were turned off and the gate valve was opened to return the system to its base pressure. The substrate holder was allowed cool for approximately sixty minutes before removing. The as-deposited films were characterized by x-ray diffraction, scanning electron microscopy, energy dispersive electron spectroscopy, x-ray photoelectron spectroscopy, x-ray reflectivity and vibrational sample magnetometry.

B. X-ray Diffraction

X-ray diffraction (XRD) analysis was performed on a Bruker D8 Advance diffractometer equipped with a Göbel mirror in the grazing incidence geometry. The angle of incidence (α) was set to 1° and 2θ scans were recorded at a step size of 0.03° for a range of 10° to 80° . 2θ measurements were made at 40 kV x 40 mA using Cu $K\alpha$ radiation (λ -1.5418 Å). The phase identification was made using Jade 9 software (Materials Data Inc. USA) and the PDF 4+ database.

C. Scanning Electron Microscopy and Energy Dispersive X-Ray Spectroscopy

Scanning electron microscopy (SEM) analysis was performed to study the surface morphology and cross section of the thin film surfaces. All measurements were performed on a JOEL JSM-7800F Field Emission Scanning Electron microscope at an accelerating potential of 1.0 kV and a working distance of 6.0 mm. The surface morphological images reported in this thesis have been obtained at a magnification of

100kX and the cross-sectional images have been obtained at a magnification of 75kX. The thickness measurements were performed using ImageJ software. Semi-quantitative analysis was performed using energy dispersive x-ray spectroscopy (EDS) on a FEI Co. Quanta to determine the relative ratio of copper to iron in the co-sputtered thin films.

D. X-ray Photoelectron Spectroscopy

X-ray Photoelectron Spectroscopy (XPS) analysis was performed on a PHI Quantera SXM Scanning X-ray Microprobe using a Al K α (λ -1486.7 eV) monochromatic x-ray excitation and a beam size of 100 μ m. Survey scans were used to identify surface elemental composition and were collected using the following parameters; 100 μ m spot size, 26.8 W, 224 eV pass energy, 1 eV step size, and a binding energy range of 0 - 1100 eV. To determine the chemical states of the surface, high resolution scans were then acquired using an identical spot size and power as the survey scans, but the pass energy and step size was reduced to 26 eV and 0.025 eV, respectively. The binding energy values were normalized through the shift of the C (1s) peak to 284.6 eV. The measurements were accurate within a range of \pm 0.3 eV. All the survey spectra were processed using MultiPak V8 software (Ulvac-phi Inc.) and the elemental identification was performed using the NIST database and literature. The peak fitting and deconvolution of the high resolution spectra were performed using the CASA XPS software. The peaks were processed by performing an initial background subtraction using an 'Offset Shirley' type background for Fe 2p spectra and a 'Linear' type background for Cu 2p spectra. Then the Fe 2p spectra were deconvoluted using a combination of a Gaussian Lorentzian fits and Cu 2p spectra were fit using a Gaussian fit. The average estimated standard deviation of the fits for all the spectra is \pm 5 %.

E. X-ray Reflectivity

X-ray Reflectivity (XRR) measurements were performed on a Siemens D5000 Diffractometer. Before performing the actual reflectivity measurements an initial detector scan was performed at 40 kV by raising the knife edge to align the sample so that the detector receives the maximum possible intensity. After this step, the knife edge was

lowered and a series of rocking curve scans were performed until the detector intensity reduced to half the maximum possible intensity (by adjusting the sample height using the z-screw). This was to ensure that the incident beam is parallel to the sample surface. Finally the measurement was performed using a locked coupled $\theta/2\theta$ scan at a voltage of 40 kV and a current of 30 mA. The raw curves were then fitted using Leptos7 software. A tri-layer model was used to create a simulated curve for all the film samples. The top layer was accounted for by surface oxidation of the films which was followed by the main film layer and finally the interfacial layer between the film and substrate. The thickness estimated by the cross-sectional SEM was used as the initial film thickness value for modelling the thickness, density and surface and interface roughness of the films.

F. Magnetic Measurements

Magnetic measurements were obtained at 300K using a Quantum Design Physical Property Measurement System (PPMS) vibrating sample magnetometer (VSM). The films were placed in measurement sample plane for all measurements. The hysteresis loop was measured to an applied field of ± 1 kOe (7.958×10^4 A/m) in 250 Oe (1.989×10^4 A/m) increments near saturation, and decreasing to 2.5 Oe (1.989×10^2 A/m) increments when approaching coercivity to obtain accurate value of the coercive field. The raw data was corrected to remove the effects of the substrate by using the following equation:

$$M_{film}(H) = M_{total}(H) - \chi_{substrate}H \quad (1)$$

Where $\chi_{substrate}$ is the susceptibility of silicon (substrate), M_{total} (emu) is the magnetization of (film + substrate) and H is the magnetic field applied to the film. The volume of the samples was determined from the surface area of the samples used for magnetic measurements and the thickness estimated from the cross-sectional SEM images (Volume = Surface area x Thickness). The magnetization data was then normalized to volume (emu/cm³).

III. RESULTS AND DISCUSSION

A. Thin Film Processing

Iron nitride and iron-copper nitride thin films were deposited by reactive magnetron sputtering on a silicon (100) wafer with a native oxide layer, at a substrate temperature of 300°C and an argon flow rate of 50 sccm. Table I states the fabrication conditions.

Table I. Fabrication conditions for thin film samples.

Sample	Deposition Time (minutes)	Iron sputter power (W)	Copper sputter power (W)	Nitrogen flow rate (sccm)
A	90	80	-	0.6
B	120	80	-	1.2
C	60	80	-	2.5
D	120	80	-	5.0
E	120	80	10	5.0
F	120	80	20	5.0
G	120	80	30	5.0
H	90	80	40	5.0
J	120	80	20	1.2
K	90	80	40	1.2

B. X-ray Diffraction

X-ray diffraction measurements were performed on the as-deposited films. The peak positions were matched with the PDF 4+ database for identification of phases. Figure 2 shows the x-ray diffraction patterns of samples A, B, C and D fabricated at nitrogen flow rates of 0.6, 1.2, 2.5 and 5.0 sccm respectively. All these samples show a broad amorphous hump near $2\theta = 20^\circ$ which corresponds to the (100) reflection of SiO_2

and a narrow well-defined peak near 53° which corresponding to (112) reflection of silicon (substrate peak). The peak positions, phases and full width at half maximum (FWHM) values for the thin film peaks of samples A, B, C and D are tabulated in Table II. The diffraction patterns of samples C & D suggest the formation of γ' -Fe₄N phase which shows peaks near 41.2° , 47.9° and 70.1° , 2θ . These peaks correspond to the (111), (200) and (220) respectively. Thus a higher nitrogen flow rate appears to aid the formation of γ' -Fe₄N phase in agreement with previous studies⁸. It can be observed that the FWHM of the peaks corresponding to $2\theta = 41.2^\circ$ and 44.8° decreases on increasing the nitrogen flow rate from 2.5 sccm (sample C) to 5 sccm (sample D). The reason for the peak broadening at a lower nitrogen flow rate could be lattice strain, defects in the film and instrumental broadening.

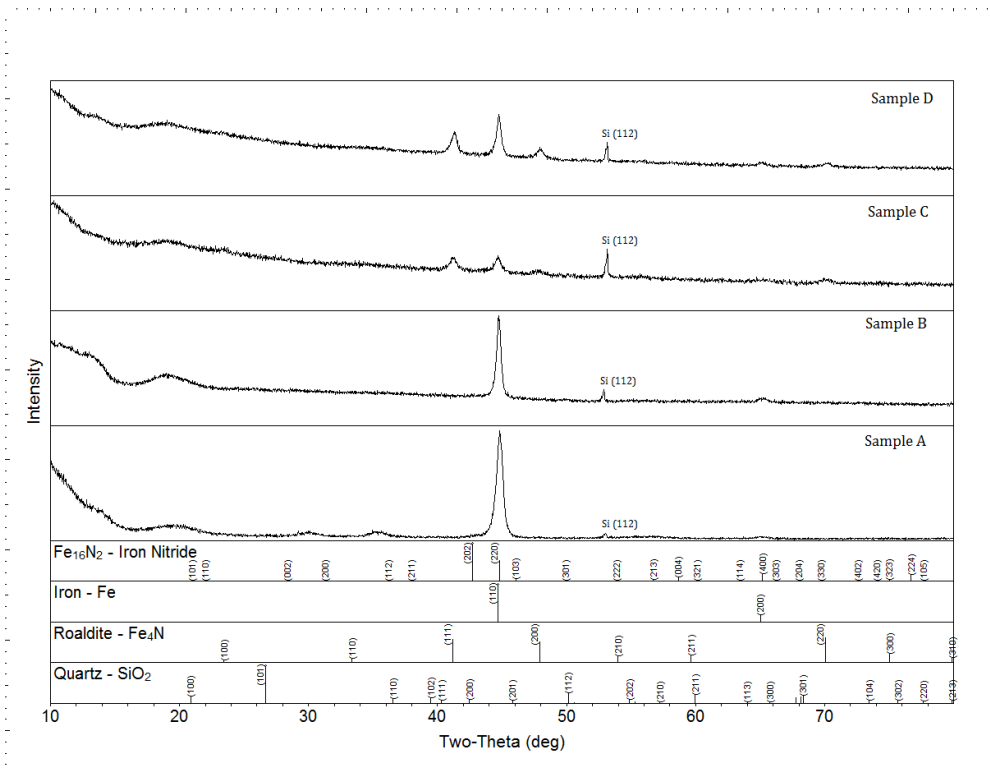


Figure 2. Stacked x-ray diffraction patterns for sample A, B, C and D.

Table II. X-ray diffraction parameters of samples A, B, C and D.

Sample	Peak position	Identified phase	FWHM
A	31.25°	α'' -Fe ₁₆ N ₂ (200)	-
	36.14°	α'' -Fe ₁₆ N ₂ (112)	-
	44.84°	α'' -Fe ₁₆ N ₂ (220) / α -Fe (110)	0.557
	54.52°	α'' -Fe ₁₆ N ₂ (222)	-
B	44.77°	α'' -Fe ₁₆ N ₂ (220) / α -Fe (110)	0.394
	65.29°	α'' -Fe ₁₆ N ₂ (400) / α -Fe (400)	-
C	41.24°	γ' -Fe ₄ N (111)	0.578
	44.72°	α'' -Fe ₁₆ N ₂ (220) / α -Fe (110)	0.453
	47.69°	γ' -Fe ₄ N (200)	0.459
	65.35°	α'' -Fe ₁₆ N ₂ (400) / α -Fe (200)	-
	69.99°	γ' -Fe ₄ N (220)	-
D	41.32°	γ' -Fe ₄ N (111)	0.463
	44.79°	α'' -Fe ₁₆ N ₂ (220) / α -Fe (110)	0.403
	48.05°	γ' -Fe ₄ N (200)	0.468
	65.06°	α'' -Fe ₁₆ N ₂ (400) / α -Fe (200)	-
	70.15°	γ' -Fe ₄ N (220)	-

The x-ray diffraction patterns for samples E, F, G and H fabricated by co-sputtering iron and copper at different copper sputtering powers and a nitrogen flow rate of 5 sccm are shown in Figure 3. The corresponding FWHM values for the thin film peaks are tabulated in Table III. The doping of copper can be attributed to the presence of a new phase (γ' -Cu_xFe_{4-x}N) whose peak positions are similar to the γ' -Fe₄N phase. This phase is formed due to the copper atoms substituting the corner and face-centered iron atoms in the γ' -Fe₄N lattice. The substitution may occur at both these sites with equal probability as these sites are equivalent. The lattice parameter for the FCC lattice of γ' -Cu_xFe_{4-x}N may have decreased with increasing copper sputtering power resulting in the shift of the XRD peaks for the (111), (200) and (220) reflections towards higher angles as observed in Figure 3. Other possible reasons for these peak shifts may be lattice strain

due to copper addition or instrumentation related errors. The (111), (200) and (220) peaks also match with the Cu_3N phase; since copper is present in these films. Figure 3 also reveals that the ratio of intensity of the peak near 41.2° to the peak near 44.8° increases as the copper sputtering power increases for sample E and sample F and the peak near 44.8° disappears for copper sputtering power of 30 W (sample G) and 40 W (sample H).

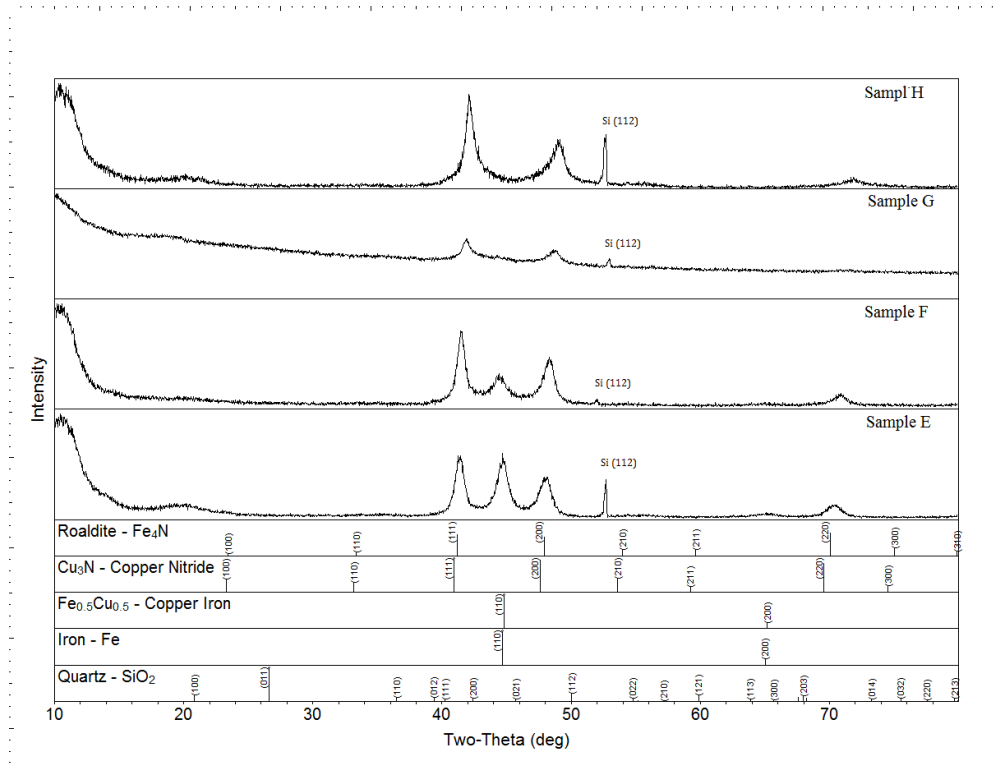


Figure 3. Stacked x-ray diffraction patterns of samples E, F, G and H.

Table III. X-ray diffraction parameters for samples E, F, G and H.

Sample	Peak position	Identified Phase	FWHM
E	41.32°	γ' -Cu _x Fe _{4-x} N / γ' -Fe ₄ N / Cu ₃ N (111)	0.723
	44.74°	Fe _{0.75} Cu _{0.25} (110) / α -Fe (110)	0.726
	48.04°	γ' -Cu _x Fe _{4-x} N / γ' -Fe ₄ N / Cu ₃ N (200)	0.780
	65.14°	Fe _{0.75} Cu _{0.25} (200) / α -Fe (200)	-
	70.45°	γ' -Cu _x Fe _{4-x} N / γ' -Fe ₄ N / Cu ₃ N (220)	-
F	41.51°	γ' -Cu _x Fe _{4-x} N / γ' -Fe ₄ N / Cu ₃ N (111)	0.597
	44.49°	Fe _{0.5} Cu _{0.5} (110) / α -Fe (110)	0.700
	48.39°	γ' -Cu _x Fe _{4-x} N / γ' -Fe ₄ N / Cu ₃ N (200)	0.828
	70.90°	γ' -Cu _x Fe _{4-x} N / γ' -Fe ₄ N / Cu ₃ N (220)	-
G	41.91°	γ' -Cu _x Fe _{4-x} N / γ' -Fe ₄ N / Cu ₃ N (111)	0.562
	48.86°	γ' -Cu _x Fe _{4-x} N / γ' -Fe ₄ N / Cu ₃ N (200)	0.741
	71.26°	γ' -Cu _x Fe _{4-x} N / γ' -Fe ₄ N / Cu ₃ N (220)	-
H	42.12°	γ' -Cu _x Fe _{4-x} N / γ' -Fe ₄ N / Cu ₃ N (111)	0.700
	49.04°	γ' -Cu _x Fe _{4-x} N / γ' -Fe ₄ N / Cu ₃ N (200)	0.629
	71.86°	γ' -Cu _x Fe _{4-x} N / γ' -Fe ₄ N / Cu ₃ N (220)	-

Figure 4 shows the x-ray diffraction patterns for samples J and K fabricated by co-sputtering iron and copper at a nitrogen flow rate of 1.2 sccm and a copper sputtering power of 20 and 40 W respectively. Table IV shows the corresponding peak positions, phases and FWHM values. The XRD pattern of sample J appears to be similar to that of sample B (Figure 2) fabricated at a nitrogen flow rate of 1.2 sccm. But, the peak near 44.8° can now be attributed to (110) reflection of Fe_{0.5}Cu_{0.5} phase since copper is present in the films along with iron. On increasing the copper sputtering power to 40 watts, sample K shows a broad peak at around 44.0°. This peak has been de-convoluted after background subtraction using a pseudo Voigt function as shown in Figure 4. The de-convoluted peaks at 43.26° and 44.48° suggest a presence of ϵ -Fe₃N, ζ -Fe₂N iron nitride phases along with copper and Fe_{0.5}Cu_{0.5}.

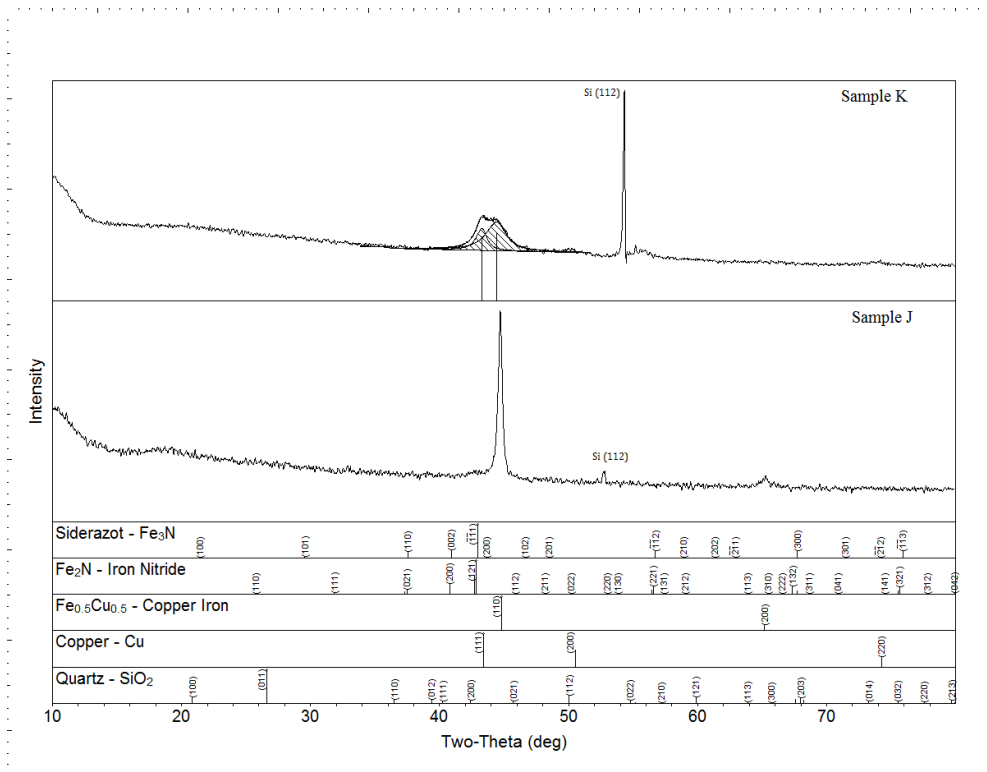


Figure 4. Stacked x-ray diffraction patterns of samples J and K.

Table IV. X-ray diffraction parameters for samples J and K.

Sample	Peak position	Identified Phase	FWHM
J	44.68°	Fe _{0.5} Cu _{0.5} (110)	0.372
	65.29°	Fe _{0.5} Cu _{0.5} (200)	-
K	43.26°	ε-Fe ₃ N ($\bar{1}$ $\bar{1}$ 1) / ζ-Fe ₂ N (121) / Cu (111)	0.976
	44.48°	Fe _{0.5} Cu _{0.5} (110)	1.845
	50.25°	Cu (200)	
	74.16°	Cu (311)	

C. Scanning Electron Microscopy and Energy Dispersive X-ray Spectroscopy

Scanning electron microscopy has been used to investigate the surface and cross-sectional morphology of the films and to determine the film thickness. All the SEM surface micrographs have been obtained at an applied voltage of 1 kV, magnification of 100kx and a working distance of 6.0 mm. Figure 5, 6, 7 and 8 show the SEM surface micrographs of samples A, B, C and D respectively. Sample A fabricated at a nitrogen flow rate of 0.6 sccm exhibits a porous surface, which is rough and has a granular morphology. The grains appear to be faceted and the grain boundaries are clearly visible. The surface shows that the grains are either stacked or grow as columns from the substrate. Sample B fabricated at a nitrogen flow rate of 1.2 sccm also shows a granular morphology but the surface appears to be relatively dense as compared to sample A. The surface also appears to be rough and shows the presence of fine grains. The surface morphology of sample C fabricated at a nitrogen flow rate of 2.5 sccm appears to be similar as sample A. The grains appear to be faceted. Increasing the nitrogen flow rate to 5 sccm the morphology of sample D shows distinct grain-like morphology. The grains appear to overlap each other and the presence of surface roughness is evident.

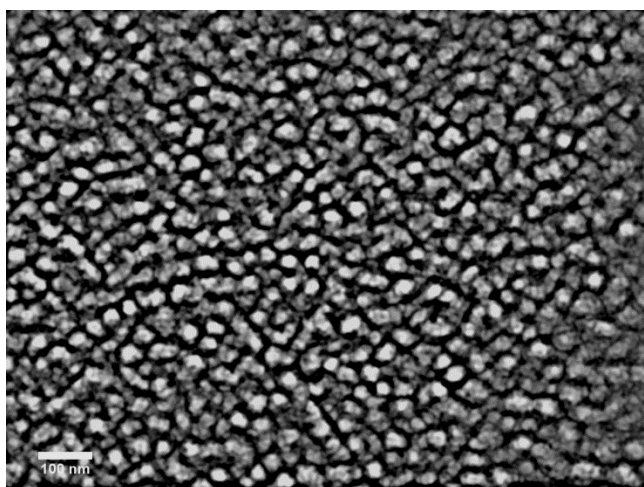


Figure 5. Representative SEM surface micrograph of sample A (scale bar - 100 nm).

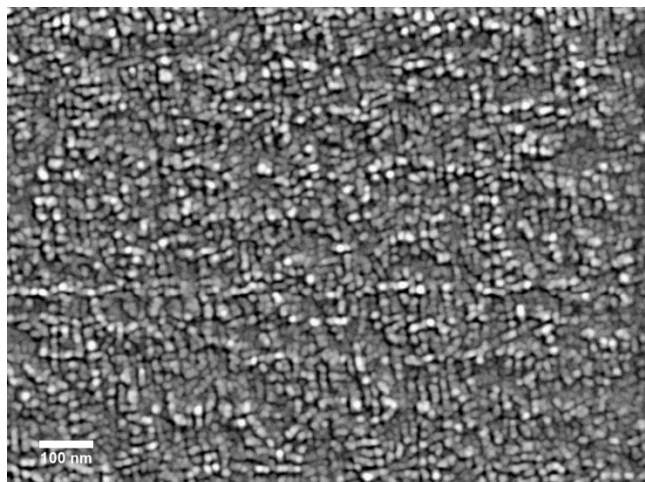


Figure 6. Representative SEM surface micrograph of sample B (scale bar - 100 nm).

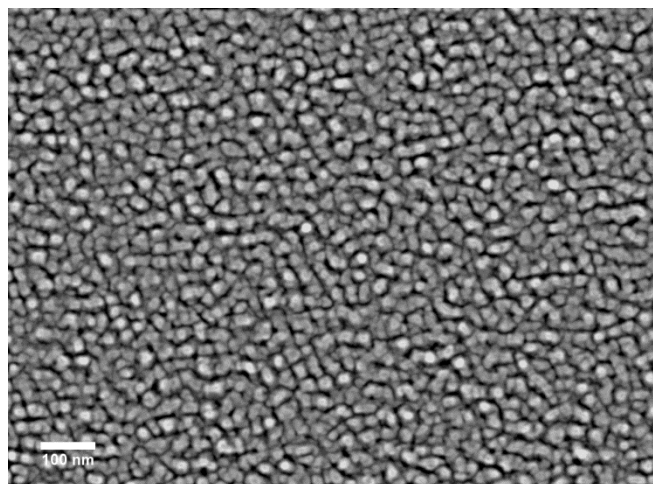


Figure 7. Representative SEM surface micrograph of sample C (scale bar - 100 nm).

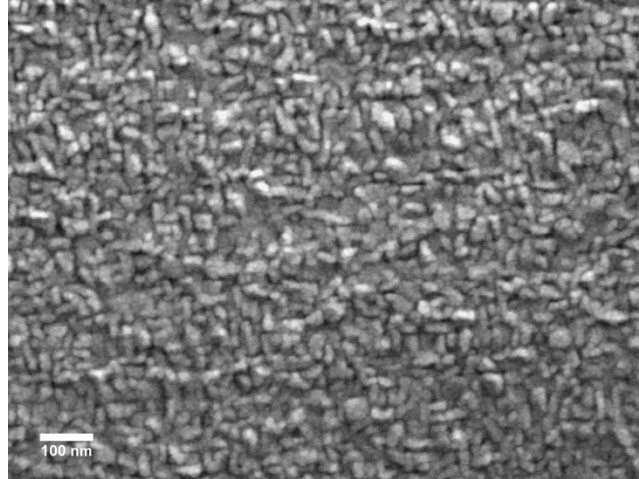


Figure 8. Representative SEM surface micrograph of sample D (scale bar - 100 nm).

Figure 9, 10, 11 and 12 show the SEM micrographs of samples E, F, G and H fabricated by co-sputtering iron and copper at a nitrogen rate of 5 sccm and different copper sputtering powers. The surface morphology of sample E and sample F shows distinct grain-like features. Both these samples show a rectangular morphology as observed from their corresponding FIB micrographs shown in appendix (Figure 56 – sample E and Figure 57 – sample F). The morphology of sample G fabricated at a copper sputtering power of 30 W shows the presence of two different phases. These phases are represented by dark and bright features as shown in Figure 58. Sample H shows a morphology which is granular comprising of equi-axed grains as shown in Figure 59. Figure 13 and 14 shows the SEM surface micrographs of the samples fabricated at a N_2 flow rate of 1.2 sccm by co-sputtering iron and copper. The surface of sample J (Cu - 20 W) suggests a preferred orientation of grains while that of sample K (Cu - 40 W) does not show this preferred orientation. The surface of both these samples appears to be dense as compared to that of sample B (Figure 6).

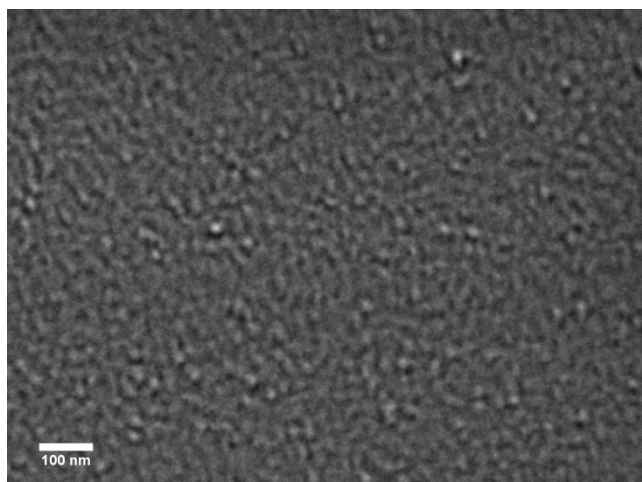


Figure 9. Representative SEM surface micrograph of sample E (scale bar - 100 nm).

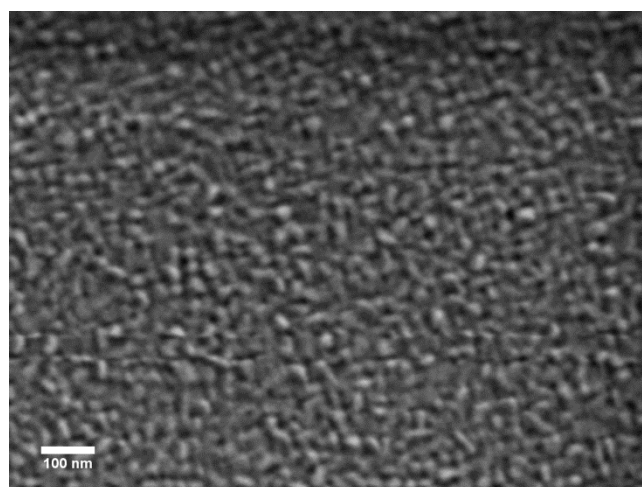


Figure 10. Representative SEM surface micrograph of sample F (scale bar - 100 nm).

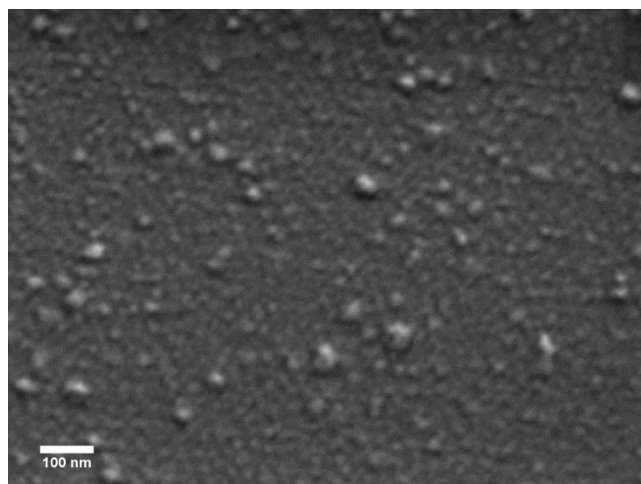


Figure 11. Representative SEM surface micrograph of sample G (scale bar - 100 nm).

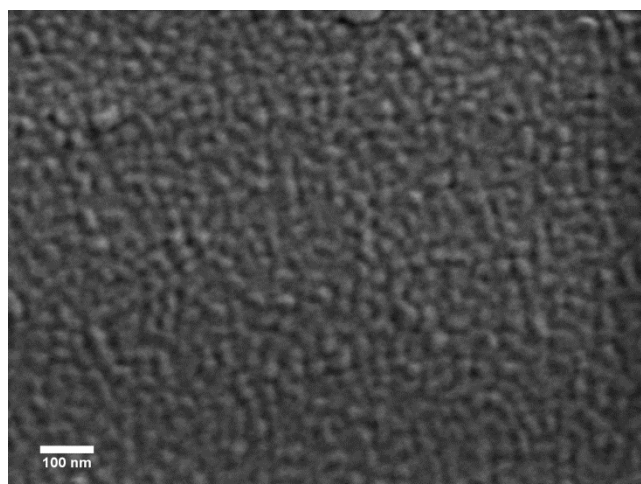


Figure 12. Representative SEM surface micrograph of sample H (scale bar - 100 nm).

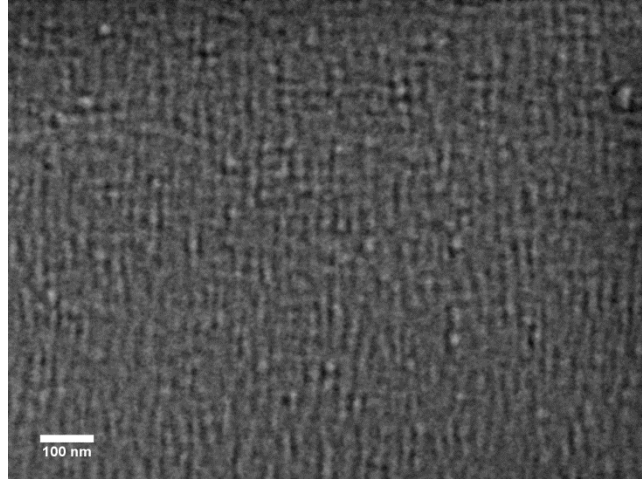


Figure 13. Representative SEM surface micrograph of sample J (scale bar - 100nm).

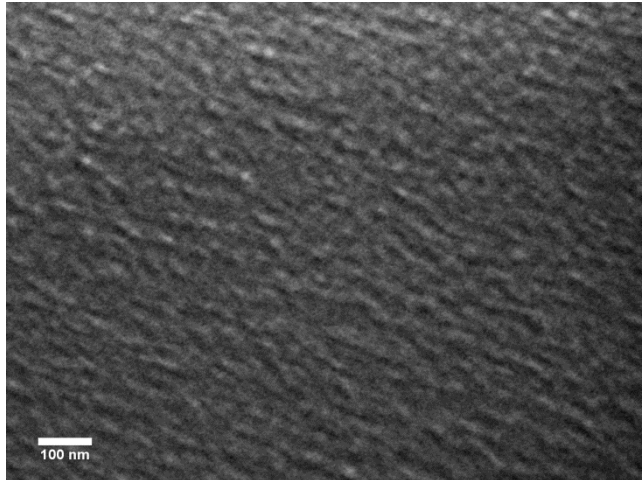


Figure 14. Representative SEM surface micrograph of sample K (scale bar - 100 nm).

All the cross-sectional SEM measurements are obtained at a voltage of 1 kV and a magnification of 75kx. The thicknesses of the as deposited thin films were measured from the cross-section are tabulated in Table V. The cross – sectional SEM micrographs of the samples A, B, C and D are shown in Figure 15, 16, 17 and 18 respectively. The columns appear to grow from the substrate but are truncated intermittently at different heights before reaching the surface of the film. Similar growth with intermittently truncated columns is also observed for the co-sputtered films; samples E, F, and G (Figure 19, 20, 21) and for sample J (Figure 23). Sample G fabricated at a copper sputtering power of 30 watts (Figure 21) shows thinner well defined columns. On increasing the copper sputter power to 40 watts, the cross-sectional SEM micrographs of samples H and K do not show columnar growth morphology and exhibit a rather homogenous cross-section.

Table V. Thicknesses of thin film samples as measured from cross-sectional SEM images.

Sample	Thickness \pm 15.0 (nm)
A	180.0
B	215.0
C	120.0
D	200.0
E	225.0
F	240.0
G	310.0
H	240.0
J	225.0
K	180.0

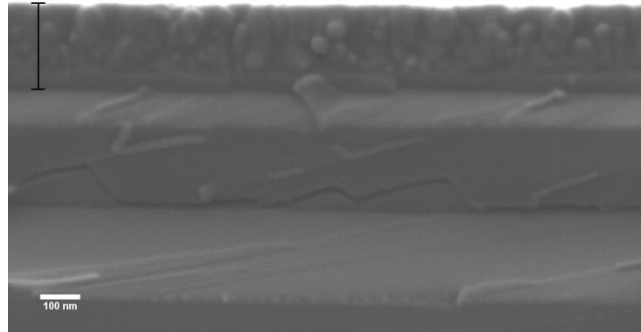


Figure 15. Cross-sectional SEM micrograph of sample A (scale bar - 100 nm).

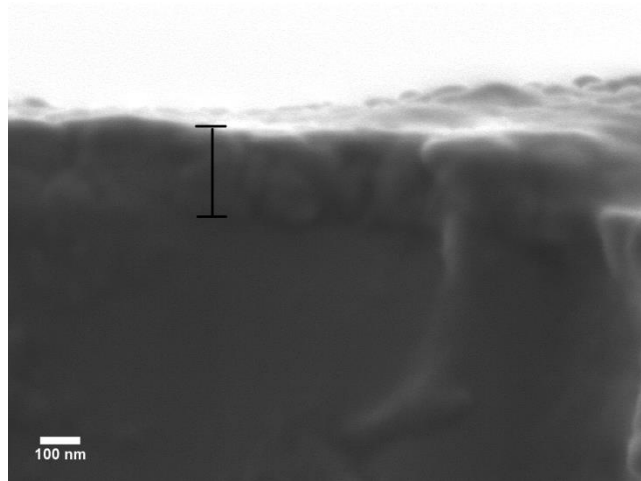


Figure 16. Cross-sectional SEM micrograph of sample B (scale bar - 100 nm).

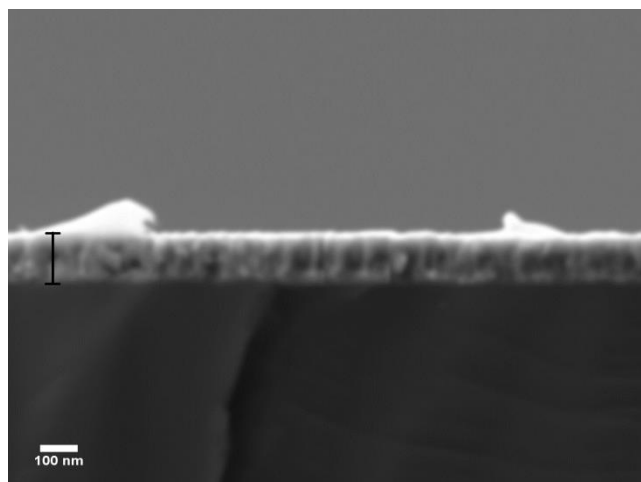


Figure 17. Cross-sectional SEM micrograph of sample C (scale bar – 100 nm).

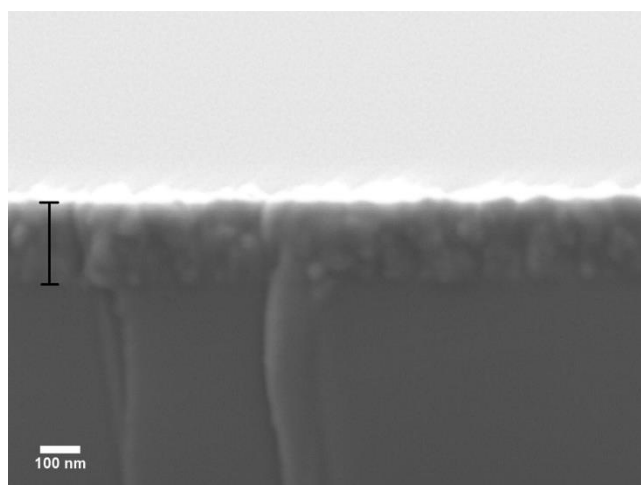


Figure 18. Cross-sectional SEM micrograph of sample D (scale bar - 100 nm).

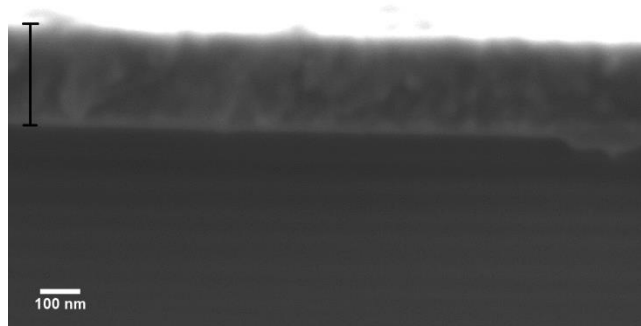


Figure 19. Cross-sectional SEM micrograph of sample E (scale bar - 100 nm).



Figure 20. Cross-sectional SEM micrograph of sample F (scale bar - 100 nm).

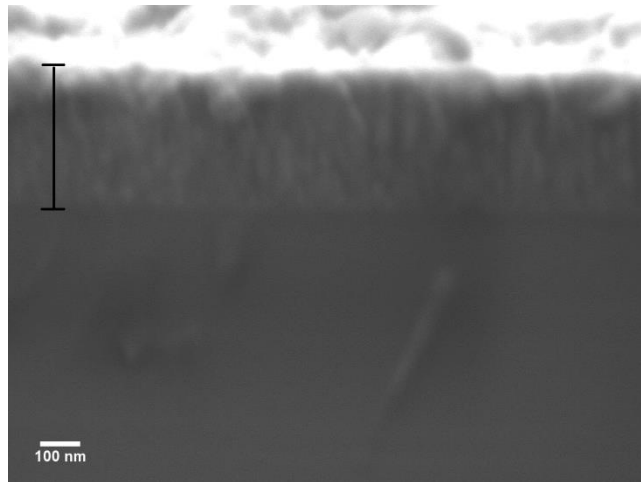


Figure 21. Cross-sectional SEM micrograph of sample G (scale bar - 100 nm).

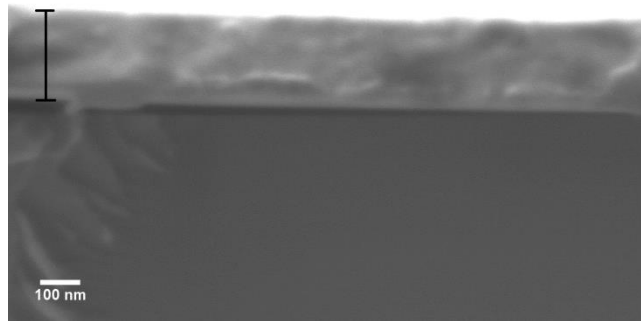


Figure 22. Cross-sectional SEM micrograph of sample H (scale bar - 100 nm).

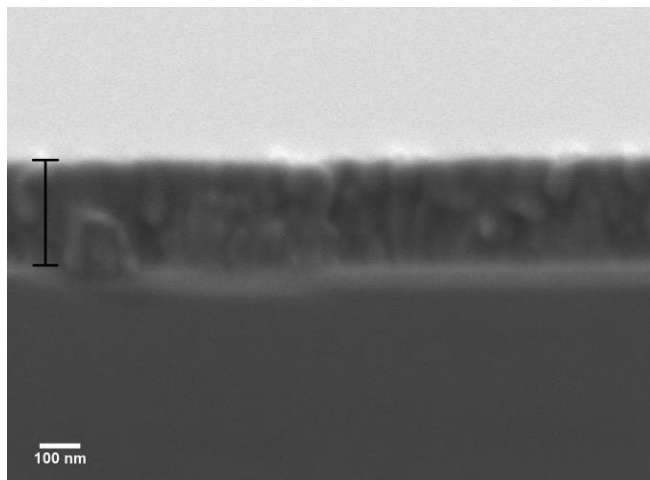


Figure 23. Cross-sectional SEM micrograph of sample J (scale bar - 100 nm).

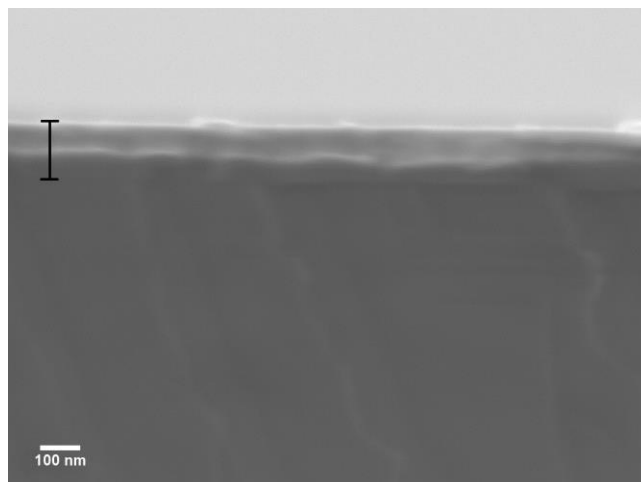


Figure 24. Cross-sectional SEM micrograph of sample K (scale bar - 100 nm).

Energy dispersive x-ray spectroscopy (EDS) was used to analyze the composition of all the films. The spectra were obtained from three different spots on the thin film surfaces and the films were confirmed to be tri-point homogeneous. The EDS spectra (not shown here) for all the iron nitride films (samples A, B, C and D) show the presence of Fe, N, O, C and Si. The spectra for the co-sputtered films (samples E, F, G, H and K) show the presence of Cu in addition to the elements detected for the iron nitride films. The signal from the substrate (Si) is also recorded since the films are thin as compared to the penetration depth (~ 500 – 600 nm) of the electron source used for EDS analysis. The values of the relative atomic ratio of copper to iron for the co-sputtered films are shown in Table VI. They have been obtained by first measuring the absolute peak intensities of L-level emission lines for iron and copper and subtracting the corresponding background intensity. Then calculating the value of $\text{Cu (L)}/[\text{Cu (L)} + \text{Fe (L)}]$. These values are obtained for all the three spots on each films and an average of these values is reported. It can be observed that for the films fabricated at nitrogen flow rates of 5 and 1.2 sccm, increasing the copper sputter power increases the relative atomic ratio of copper.

Table VI. Relative atomic ratio of copper in the iron-copper nitride films.

Thin Film ID	Cu (watts)	Cu / (Cu + Fe)
E	10	0.14
F	20	0.29
G	30	0.40
H	40	0.48
J	20	0.29
K	40	0.48

D. X-ray Photoelectron Spectroscopy

In order to get rid of the surface impurities and to fabricate contaminant free films, all the targets were pre-sputtered in vacuum prior to the start of the deposition experiment. The high resolution scans for the iron and copper sputtering targets are shown in Figure 25 and 26 respectively. Two distinct peaks at binding energies 706.5 eV and 719.8 eV are observed in the Fe 2p spectrum of the iron target, which correspond well with the Fe 2p_{3/2} and Fe 2p_{1/2} peaks for Fe metal⁴². Similarly, the Cu 2p spectrum of the copper target shows two distinct peaks at 932.5 eV and 952.3 eV corresponding to the Cu 2p_{3/2} and Cu 2p_{1/2} peaks of Cu metal as suggested by the NIST database.

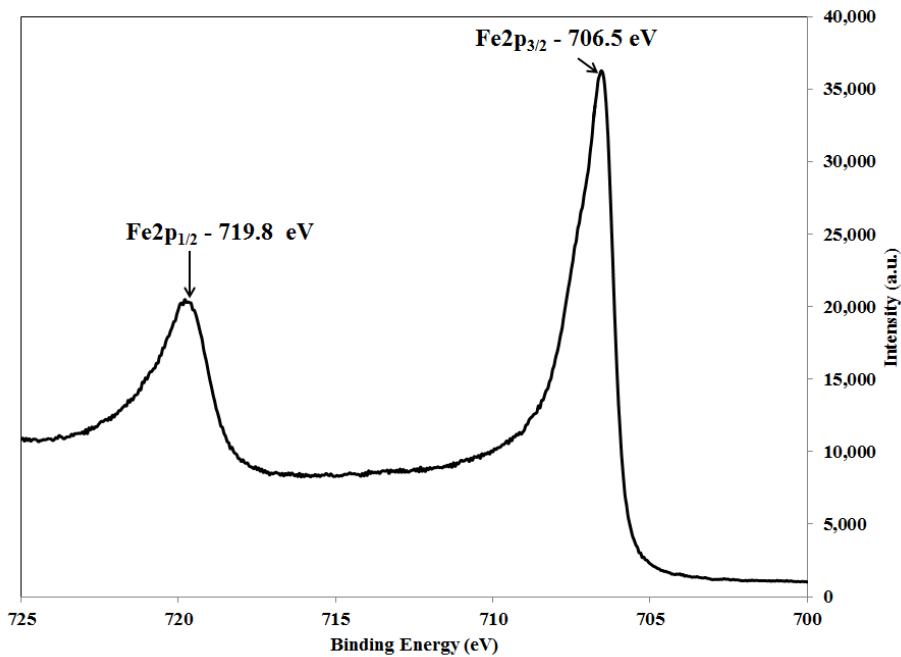


Figure 25. High resolution XPS spectrum for the Fe 2p region of the iron sputtering target after Ar⁺ sputtering to remove contaminants.

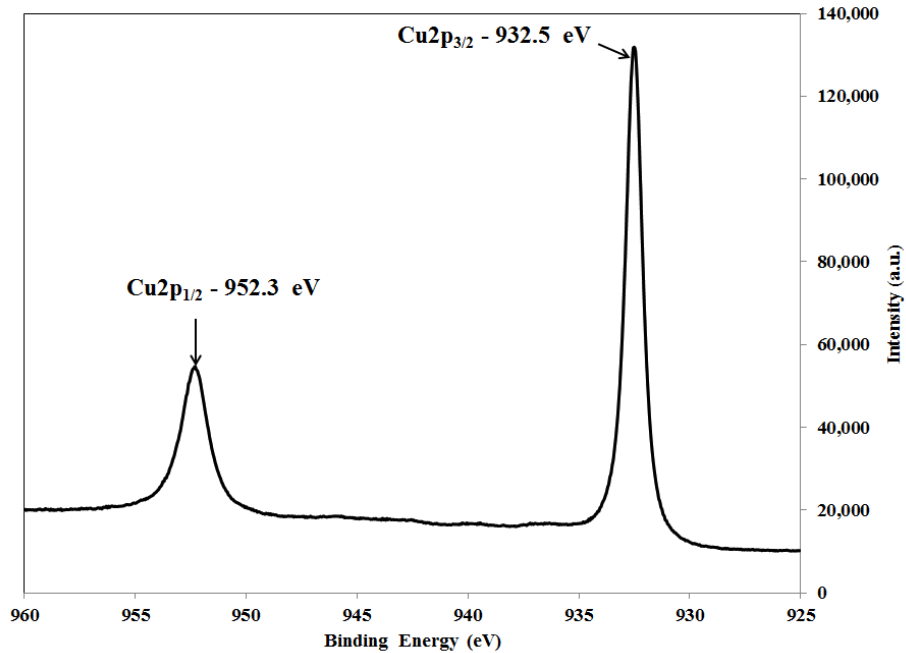


Figure 26. High resolution XPS spectrum for the Cu 2p region of the iron sputtering target after Ar⁺ sputtering to remove contaminants.

Figure 27 shows the XPS survey spectra for samples A, B, C and D. All these films show core level peaks for iron, oxygen, and carbon along with the Auger peaks for iron (Fe LMM) and oxygen (O KLL). The high intensity oxygen peak (O 1s) suggests that the film have undergone surface oxidation due to exposure to an O₂ rich ambient environment. The spectrum of sample A also shows the core level peak for argon which might have been absorbed or penetrated the surface during XPS measurements. The nitrogen core level peak near 400 eV is not visible in the spectra probably due to the presence of the high intensity oxygen peak. The survey spectra of the co-sputtered films fabricated at nitrogen flow rates of 5 sccm and 1.2 sccm are shown in Figure 28 and 29 respectively. Apart from the core level peaks for iron, oxygen and carbon, the spectra also show Auger peak for copper (Cu LMM).

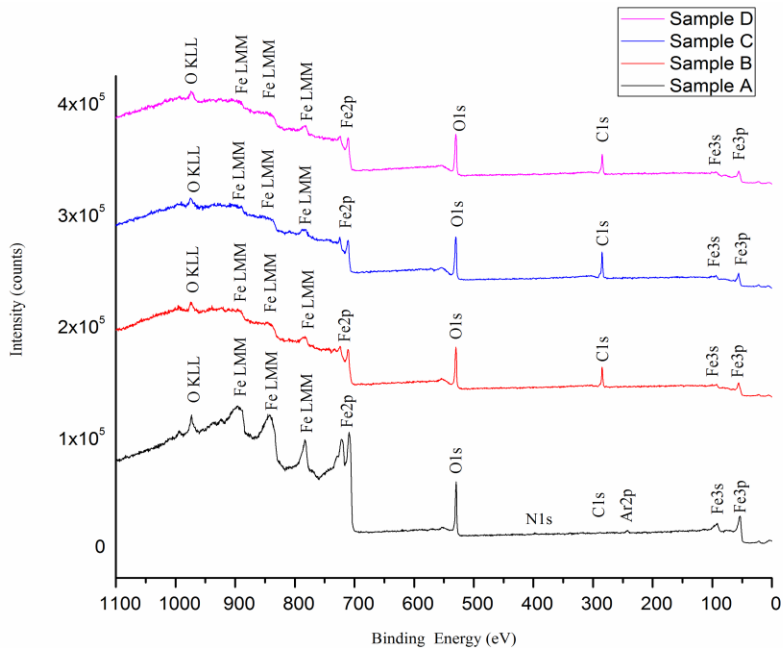


Figure 27. XPS survey spectra for samples A, B, C and D.

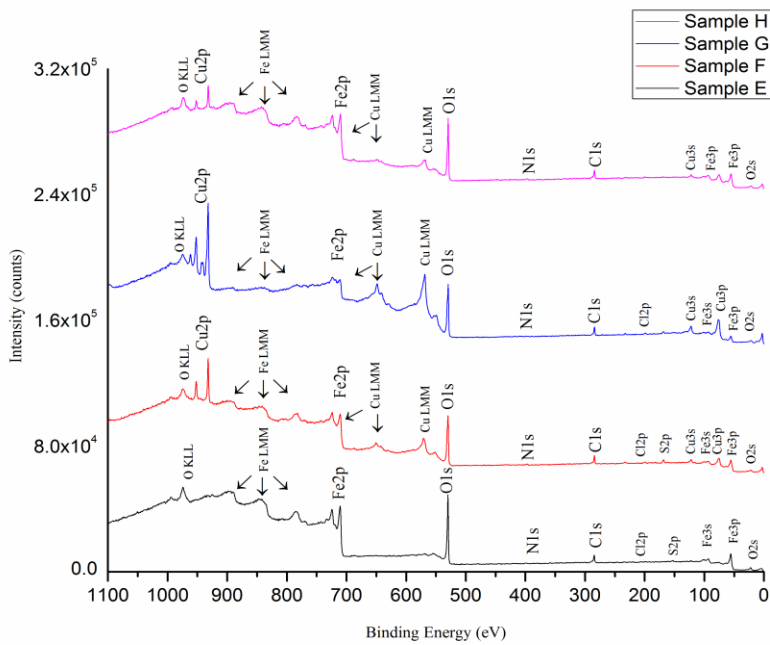


Figure 28. XPS survey spectra for samples E, F, G and H.

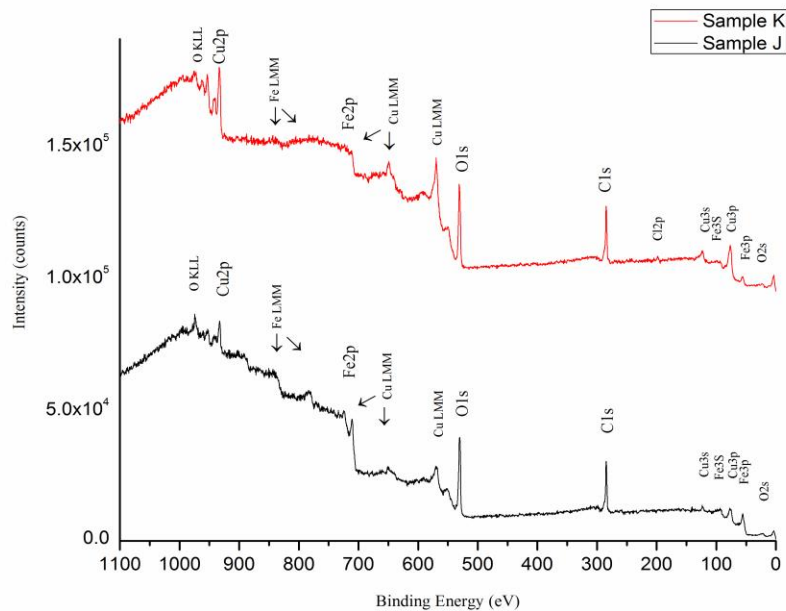


Figure 29. XPS survey spectra for samples J and K.

In order to further investigate the surface oxidation phenomena in the films, high resolution XPS spectra were recorded for the Fe 2p region of the pure iron nitride films and the Fe 2p and Cu 2p regions of the co-sputtered films. All these spectra were then background subtracted and deconvoluted using suitable peak fitting parameters as described in the experimental section. The spectra for the Fe 2p region of samples A, B, C and D are shown in Figure 30, 31, 32 and 33. The deconvoluted peak positions and the characteristics of the deconvoluted peaks are tabulated in Table VII. The deconvolution of the Fe 2p_{3/2} region revealed the presence of three peaks. The peak at the lowest binding energy is located at 707.4 eV, 707.0 eV, 707.7 eV and 707.1 eV for samples A, B, C and D, respectively. Comparing with the Fe 2p_{3/2} peak position for the iron sputtering target (706.5 eV), the peak showed a shift towards higher binding energy value. This can be attributed to a change in local coordination of iron in the film. Based on past literature this peak can be attributed to the presence of iron nitrides⁴³⁻⁴⁵. The next peak is located at 710.4 eV, 710.9 eV, 710.1 eV and 710.6 eV for samples A, B, C and D, respectively. These peaks can be assigned to a mixture of Fe²⁺ and Fe³⁺ oxides based on past

literature⁴² and are the main oxide peaks. Identification of a particular oxide is difficult due to the near identical binding energy values for Fe²⁺ (710.7 eV⁴²) and Fe³⁺ (710.8 eV⁴²) oxides. The presence of iron oxide can be further confirmed by the Fe 2p_{3/2} satellite peak located 8 - 9 eV higher than main oxide peak^{42,46}. The deconvoluted spectra show a third peak for the Fe 2p_{3/2} region which aids the fitting process of the spectra.

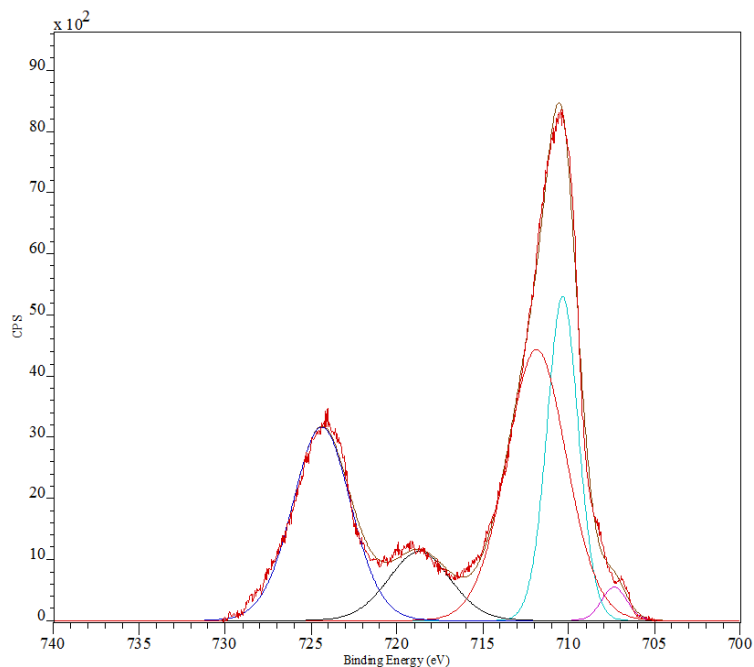


Figure 30. High resolution XPS spectrum for the Fe 2p region of sample A.

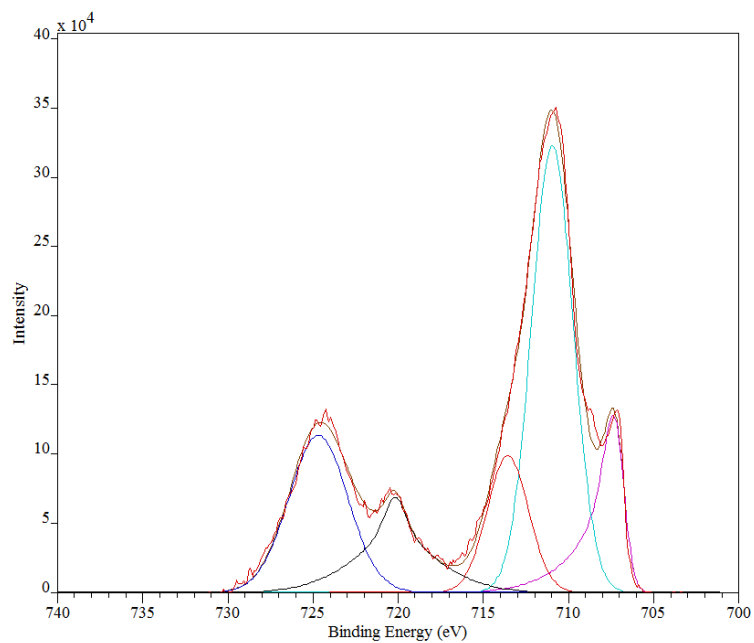


Figure 31. High resolution XPS spectrum for the Fe 2p region of sample B.

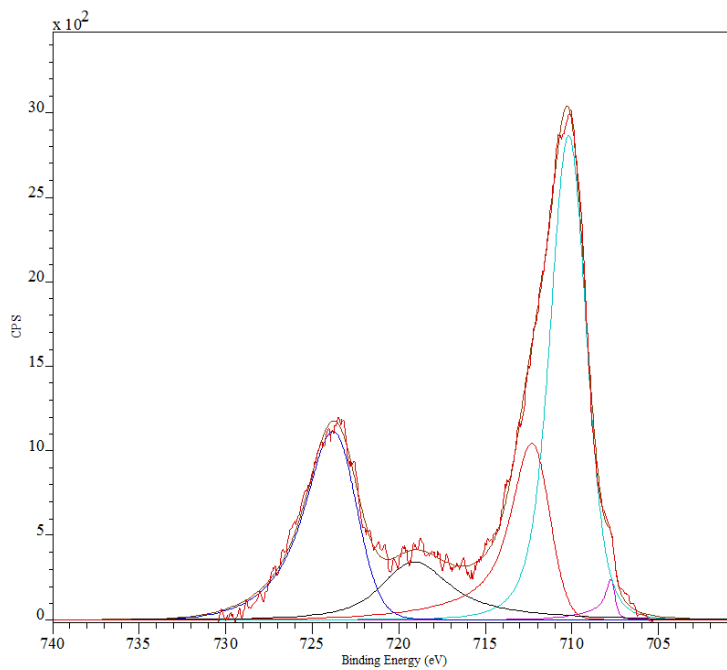


Figure 32. High resolution XPS spectrum for the Fe 2p region of sample C.

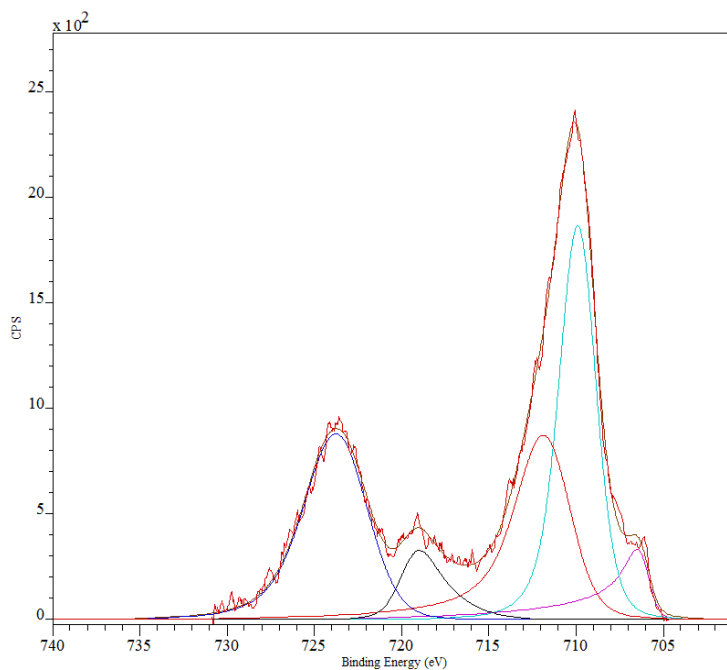


Figure 33. High resolution XPS spectrum for the Fe 2p region of sample D.

Table VII. Deconvoluted peak parameters for the Fe 2p region of samples A, B, C and D.

Sample A	Sample B	Sample C	Sample D	Peak Characteristic
Binding Energy (eV) \pm 0.3 eV				
707.4	707.0	707.7	707.1	Fe 2p _{3/2} – Iron nitride
710.4	710.9	710.1	710.6	Fe 2p _{3/2} – Main iron oxide peak
711.9	713.4	712.0	713.3	Fe 2p _{3/2} - Iron oxide
718.7	720.1	719.3	719.8	Fe 2p _{3/2} - Satellite
724.4	724.6	723.4	724.2	Fe 2p _{1/2} – Iron Oxide

Figure 34, 35, 36 and 37 show the spectra for the Fe 2p region of samples E, F G and H respectively. The corresponding deconvoluted peak positions and the characteristics of the deconvoluted peaks are tabulated in Table VIII. The peak corresponding to iron nitrides (~ 707 eV) which was present for samples A, B, C and D is not visible in the deconvoluted spectra for the co-sputtered films E, F, G and H. The first set of peaks are observed at 710.2 eV, 710.3 eV, 710.8 eV and 710.9 eV which confirm the presence of a mixed iron oxides (Fe^{2+} and Fe^{3+}) similar to samples A, B, C and D.

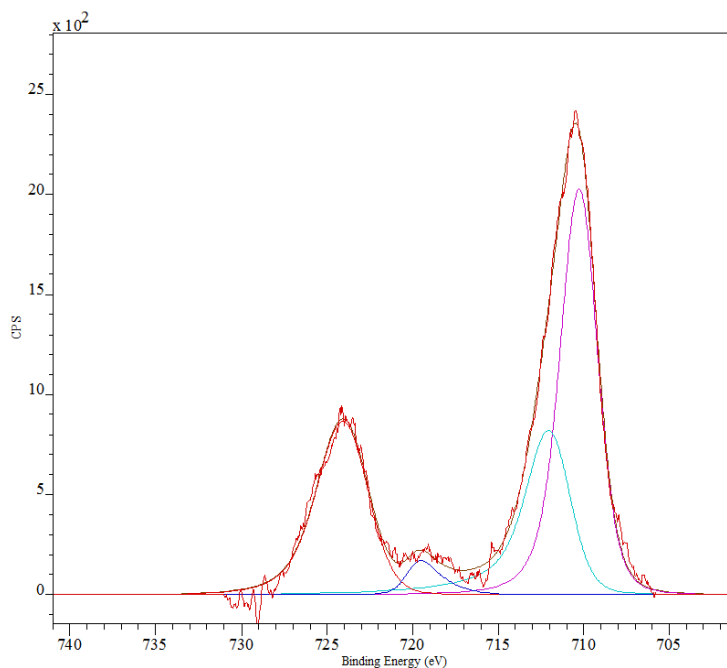


Figure 34. High resolution XPS spectrum for the Fe 2p region of sample E.

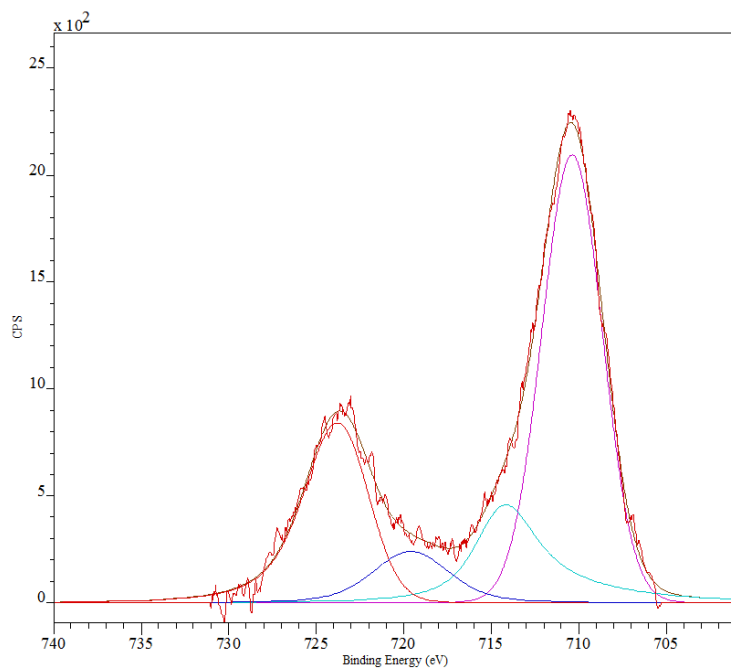


Figure 35. High resolution XPS spectrum for the Fe 2p region of sample F.

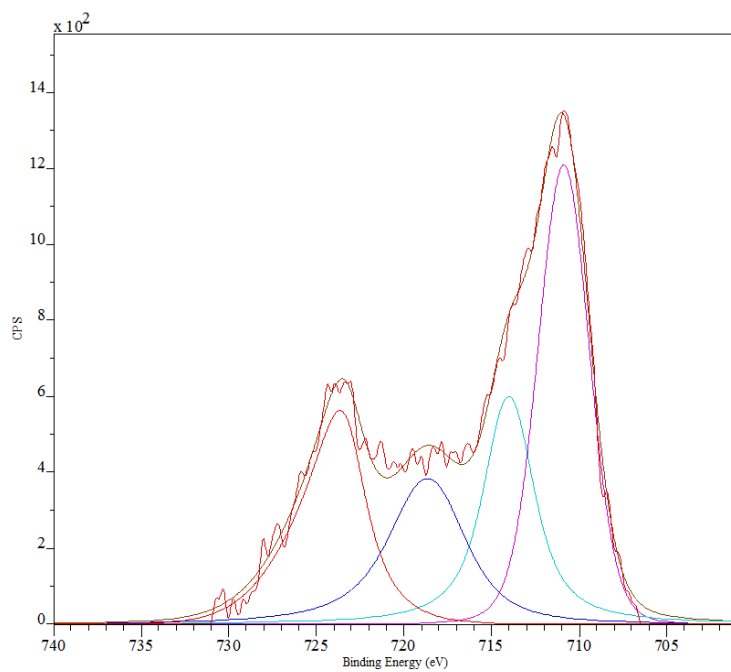


Figure 36. High resolution XPS spectrum for the Fe 2p region of sample G.

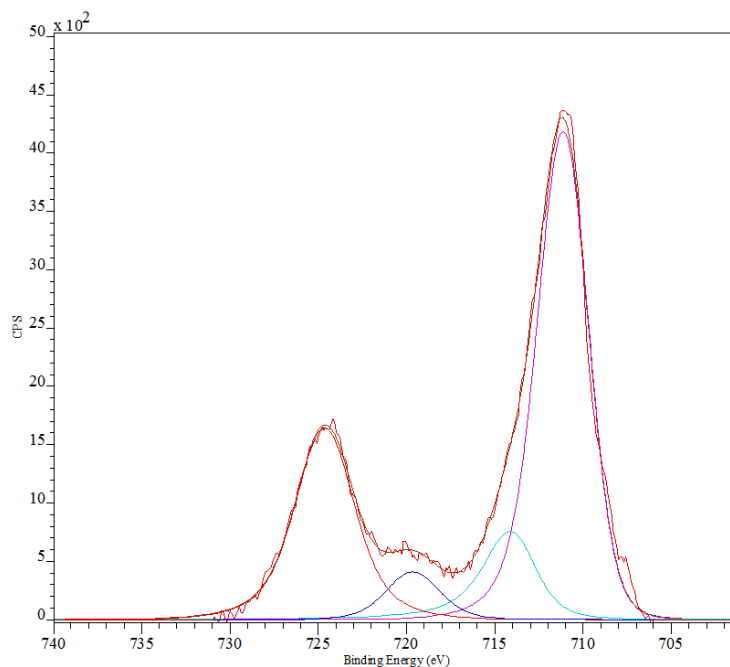


Figure 37. High resolution XPS spectrum for the Fe 2p region of sample H.

Table VIII. Deconvoluted peak parameters for the Fe 2p region of samples E, F, G and H.

Sample E	Sample F	Sample G	Sample H	Peak Characteristic
Binding Energy (eV) \pm 0.3 eV				
710.2	710.3	710.8	710.9	Fe 2p _{3/2} – Main iron oxide peak
711.8	714.3	714.0	714.0	Fe 2p _{3/2} – Iron oxides
719.8	719.6	718.6	719.7	Fe 2p _{3/2} - Satellite
724.0	723.4	723.5	724.6	Fe 2p _{1/2} – Iron oxides

The high resolution spectra of Sample E does not show a peak corresponding to the Cu 2p presumably due to low copper sputtering power (Cu – 10 watts) used for fabrication in this film. The high resolution spectra for the Cu 2p region of the samples F, G and H are shown in Figure 38, 39 and 40 and the corresponding peak positions are tabulated in Table IX. The Cu 2p_{3/2} peaks are located at 932.6 eV, 932.6 eV and 933.3 eV for samples F, G, and H respectively. On comparing with the Cu 2p_{3/2} peak position of the copper sputtering target, the peaks do not show a shift for samples F and G. Thus these peaks also belong to metallic copper. On increasing the copper sputter power to 40 watts the Cu 2p_{3/2} peak shifts to a higher binding energy value of 933.3 eV and based on past literature can be assigned to the Cu₃N⁴⁷.

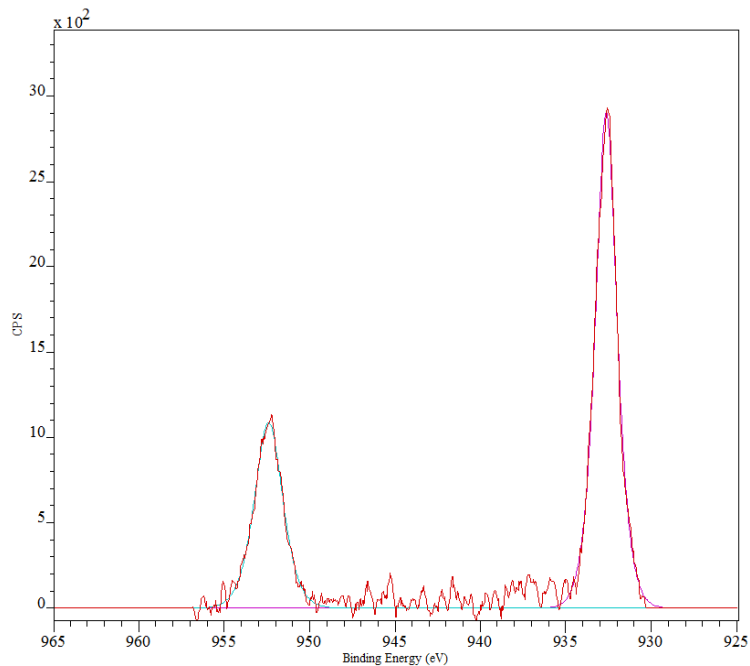


Figure 38. High resolution XPS spectrum for the Cu 2p region of sample F.

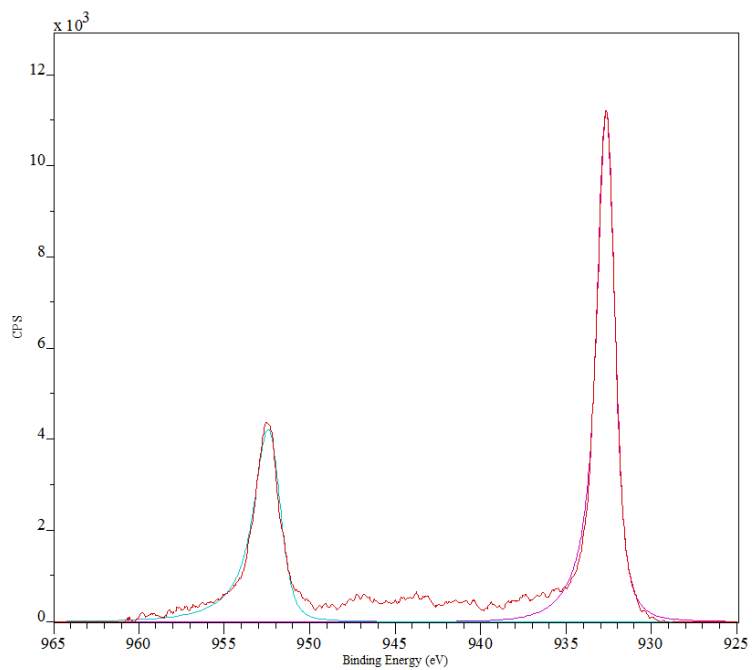


Figure 39. High resolution XPS spectrum for the Cu 2p region of sample G.

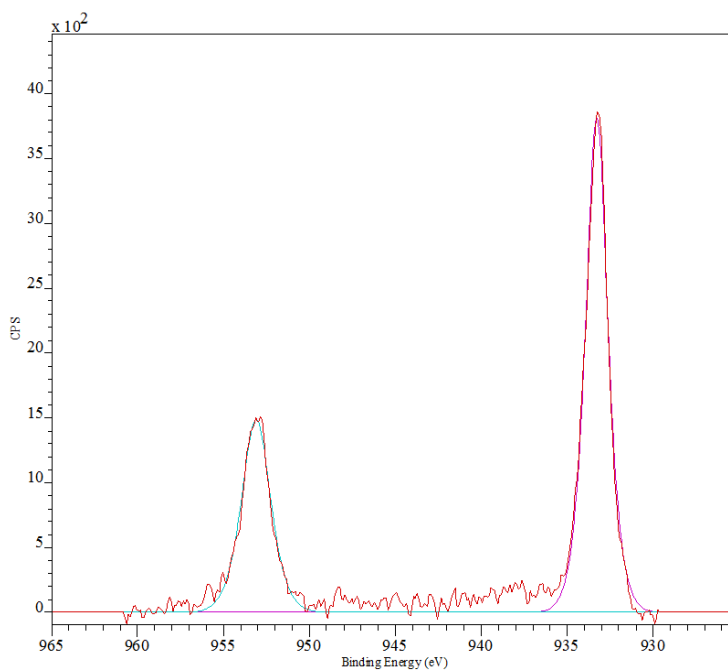


Figure 40. High resolution XPS spectrum for the Cu 2p region of sample H.

Table IX. Binding energy values of the Cu 2p region of samples F, G and H.

Sample F	Sample G	Sample H	Peak Characteristic
Binding Energy (eV) \pm 0.3 eV			
932.6	932.6	933.3	Cu 2p _{3/2} – Cu metal / Cu ₃ N
952.4	952.3	953.1	Cu 2p _{1/2} - Cu metal / Cu ₃ N

The high resolution spectra for the Fe 2p region of sample J and K are shown in Figure 41 and 42 respectively and the deconvoluted peak positions are tabulated in Table X. The spectra show the presence of Fe²⁺ and Fe³⁺ oxides previously observed for other samples. The Cu 2p high resolution spectra for these samples are shown in Figure 43 and 44 respectively. The positions of the Cu2p_{3/2} peaks are 932.6 eV and 932.7 eV for samples J and K respectively and they are assigned to metallic copper as shown in Table XI.

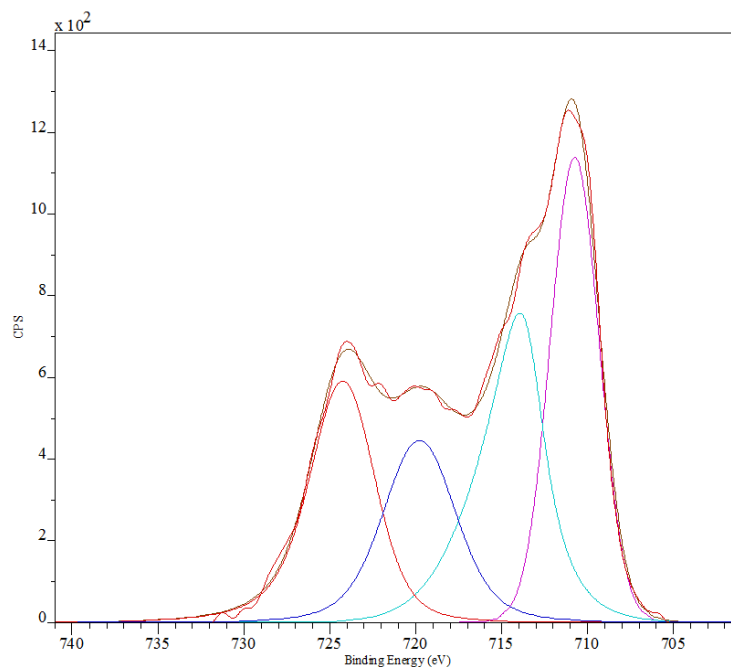


Figure 41. High resolution XPS spectrum for the Fe 2p region of sample J.

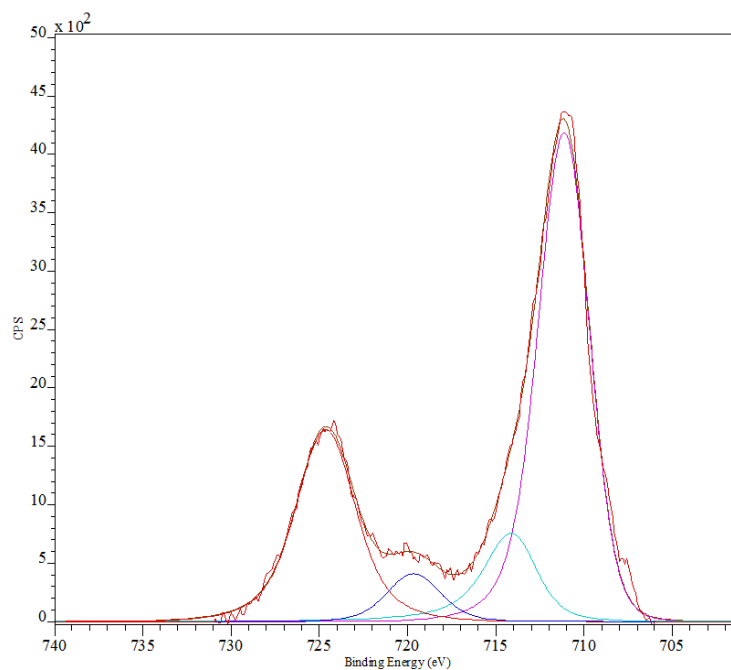


Figure 42. High resolution XPS spectrum for the Fe 2p region of sample K.

Table X. Binding energy values for the Fe 2p region of samples J and K.

Sample J	Sample K	Peak Characteristics
Binding Energy (eV) \pm 0.3 eV		
710.3	710.7	Fe 2p _{3/2} – Iron Oxides
712.9	713.8	Fe 2p _{3/2} – Iron Oxides
719.1	719.8	Fe 2p _{3/2} - Satellite
723.7	724.1	Fe 2p _{1/2} – Iron Oxides

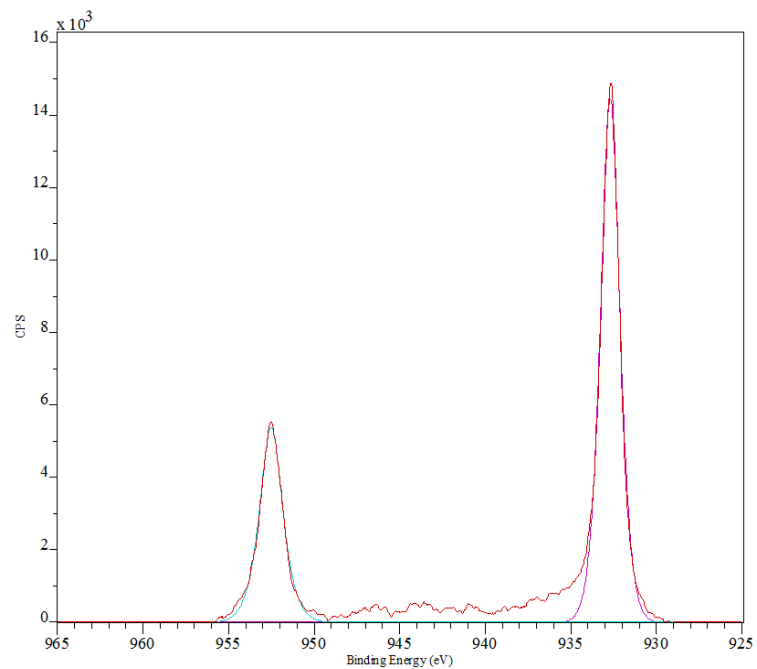


Figure 43. High resolution XPS spectrum for the Cu 2p region of sample J.

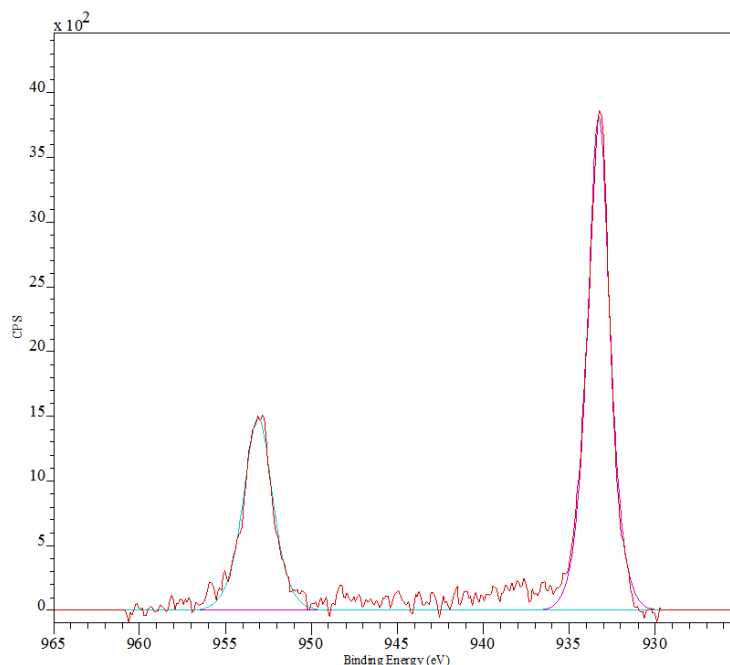


Figure 44. High resolution XPS spectrum for the Cu 2p region of sample K.

Table XI. Binding energy values for the Cu 2p region of samples J and K.

Sample J	Sample K	Peak Characteristics
Binding Energy (eV) \pm 0.3 eV		
932.6	932.7	Cu 2p _{3/2} – Cu metal
952.4	952.5	Cu 2p _{1/2} – Cu metal

E. X-Ray Reflectivity

X-ray reflectivity (XRR) modelling was performed on Leptos7 software using a tri-layered model for all the thin films. The top layer was assumed to be a surface oxide layer which was followed by the main thin film layer and then the interfacial layer between the film and the substrate. The model was found to be a good-fit as compared to a single layered model of iron nitride layer for the raw XRR curves (measured curves) and confirmed the presence of three distinct layers in the film.

The raw and the simulated reflectivity data for samples A, B, C, and D are shown in Figure 45 and the corresponding fitting results are presented in Table XII. Sample A ($N_2 = 0.6$ sccm) shows a sharp decay in the reflected intensity towards higher angles, suggesting a large surface roughness. The fitted parameter data shows a surface roughness value of 6.26 ± 0.1 nm. The SEM surface micrograph for the sample (Figure 5) shows that the surface of the film is porous. Thus the surface roughness could be attributed to the presence of voids on the surface. The simulated curve for sample A, shows the presence of low amplitude Kiessig's fringes which were not obtained for the raw curve. This might have resulted in a discrepancy for the thickness measured by cross-sectional SEM (~ 180 nm) and predicted by XRR (~ 216 nm). The raw reflectivity pattern for sample B shows the presence of Kiessig's fringes which extend to higher angles. The simulated curve closely follows these fringes, thus providing a somewhat accurate prediction of the thin film thickness. As compared to sample A, the decay in the reflected intensity of sample B is more gradual thus suggesting a lower surface roughness (3.1 nm). The density of the surface layer is higher than that of sample A which is in accordance with the observations made from the surface SEM images (Figure 5 and 6). Increasing the N_2 flow rate to 2.5 sccm, the fitted parameter data for sample C predicts a very low surface roughness (0.2 nm) and a high density for the film layer (8.38 g/cm^3). The Kiessig's fringes which are observed at lower angles rapidly decrease at higher angles suggesting the presence of an interface roughness within the film which is confirmed from the fitted parameter data shown in Table XII. High amplitude Kiessig's fringes are observed in the raw reflectivity curve of sample D which is matched closely by the simulated curve. The decrease in the reflected intensity and decrease in the amplitude of the fringes might have resulted in the surface and interface roughness predicted by the fitted parameter data. Figure 46 shows a comparison between the thickness values predicted from the XRR and measured by the cross-sectional SEM images for samples A, B, C and D. Except from sample A, the predicted and measured values match closely within range of standard errors.

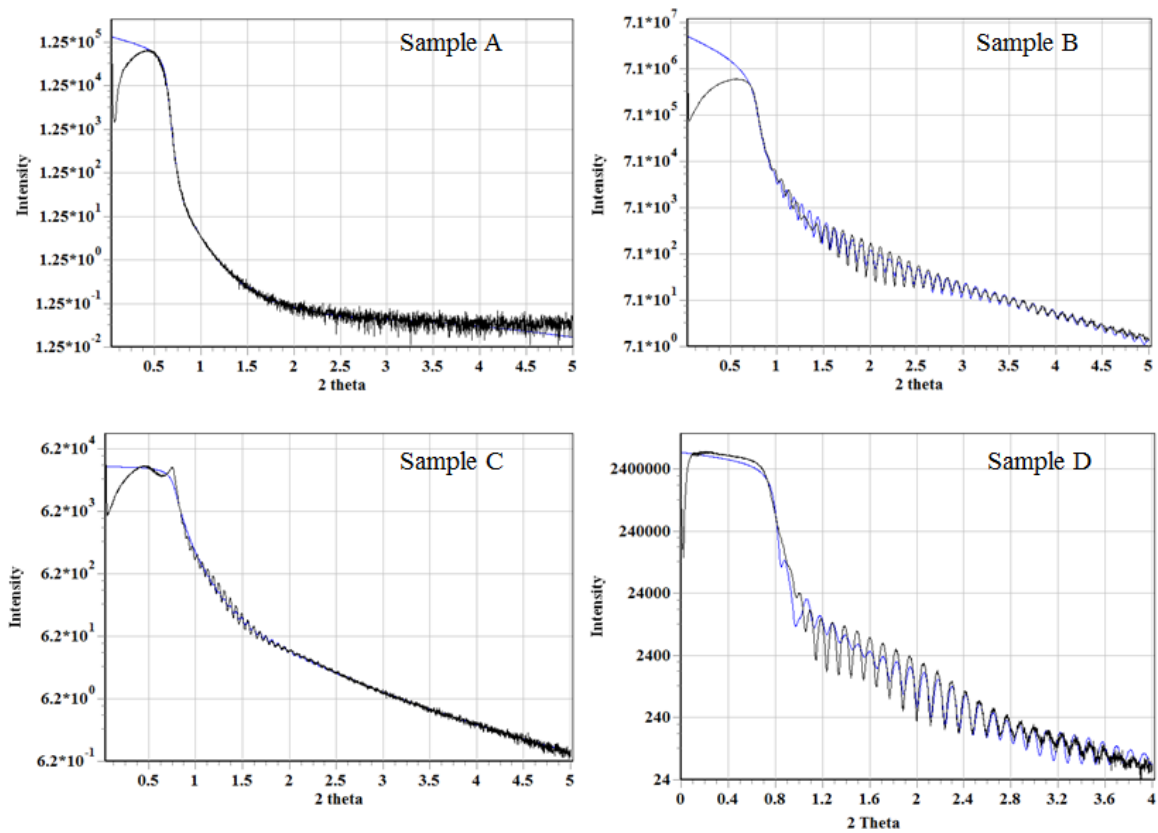


Figure 45. Raw (measured) and simulated XRR curves of samples A, B, C and D. Raw (Black), Simulated (Blue).

Table XII. XRR curve fitting parameters for samples A, B, C and D.

Sample	Layer	Thickness (nm) \pm 0.5	Roughness (nm) \pm 0.1	Density (g/cm ³) \pm 0.2
A	Surface layer	1.0	6.26	5.81
	Film layer	215.6	1.05	5.71
	Interfacial layer	1.7	0.01	3.80
B	Surface layer	6.2	3.1	6.40
	Film layer	198	0.3	7.80
	Interfacial layer	5.1	0.9	2.90
C	Surface layer	2.6	0.20	6.62
	Film layer	119.1	1.12	8.38
	Interfacial layer	0.2	1.39	2.56
D	Surface layer	3.9	3.91	5.72
	Film layer	192	1.14	7.64
	Interfacial layer	1.6	0.73	2.71

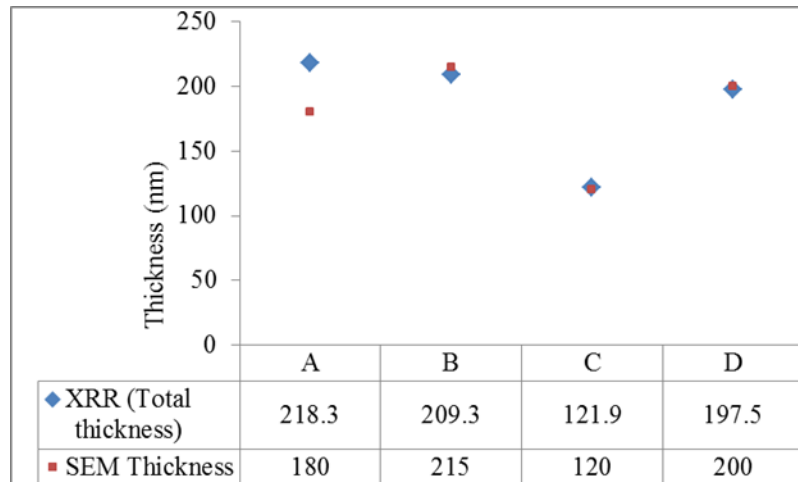


Figure 46. Thickness comparison of samples A, B, C and D predicted from XRR curve fitting (total thickness - all three layers) and cross-sectional SEM measurements.

Figure 47 shows the raw and simulated reflectivity curves for samples E, F, G and H fabricated at a N_2 flow rate of 5 sccm and increasing copper sputtering powers. Table XIII shows the corresponding fitted parameter data for these samples. Similar to the iron nitride films, the curve fitting model confirms the presence of a surface oxide layer, film layer and an interfacial layer in these films. Compared to the reflectivity curve of sample D, all the co-sputtered films show a sharp decay in the reflected intensity with increasing incident angles. Thus, the surface roughness values for samples E (6.0 nm), F (4.48 nm) and G (4.69 nm) are higher than that of sample D (3.91 nm). But sample H shows a roughness value of 3.61 nm which is slightly lower than that of sample D. The simulated curves for all these samples match closely with the measured curves thus providing a good match between the thickness predicted from XRR and measured from cross-sectional SEM as shown in Figure 48. The reflectivity curve for samples J & K (not shown here) predict near about the same total film thickness values (Table XIV) compared with their cross-sectional SEM thickness measurements.

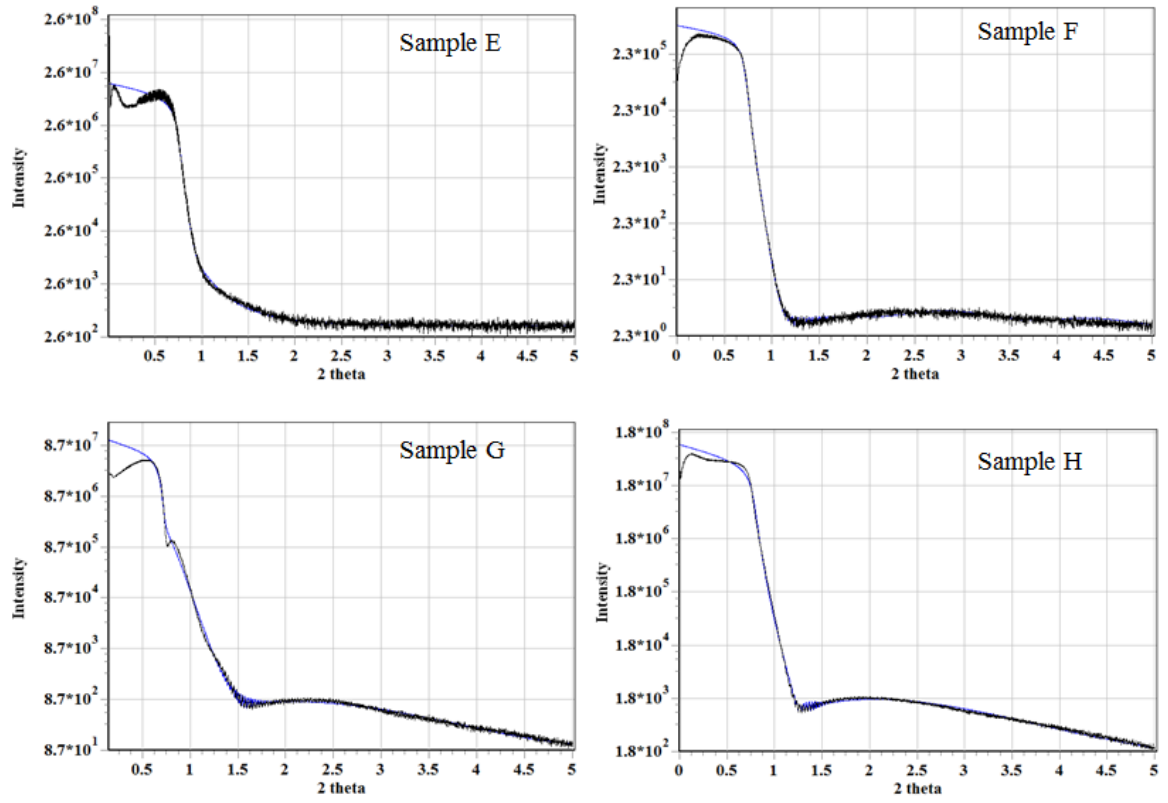


Figure 47. Raw (measured) and simulated XRR curves of samples E, F, G and H. Raw (Black), Simulated (Blue).

Table XIII. XRR curve fitting parameters for samples E, F, G and H.

Sample	Layer	Thickness (nm) \pm 0.5	Roughness (nm) \pm 0.1	Density (g/cm ³) \pm 0.2
E	Surface layer	10.4	6.0	7.8
	Film layer	185.7	0.0005	7.4
	Interfacial layer	6.6	3.2	2.4
F	Surface layer	5.4	4.48	6.78
	Film layer	239.2	2.42	6.90
	Interfacial layer	5.4	0.13	6.33
G	Surface layer	1.4	4.69	8.02
	Film layer	307.7	2.52	6.29
	Interfacial layer	2.03	0.38	0.30
H	Surface layer	4.5	3.61	5.99
	Film layer	240.9	2.57	6.44
	Interfacial layer	2.4	0.05	5.73

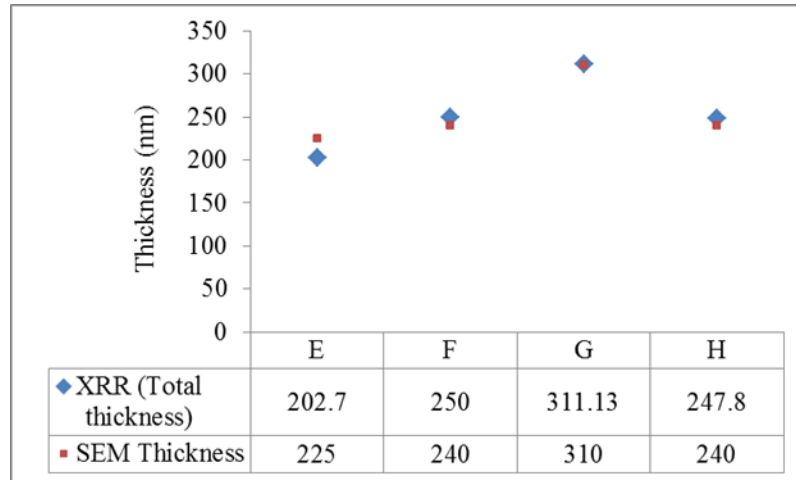


Figure 48. Thickness comparison of samples E, F, G and H predicted from XRR curve fitting of three layers and cross-sectional SEM measurement.

Table XIV. XRR curve fitting parameters for sample J and K.

Sample	Layer	Thickness (nm) \pm 0.5	Roughness (nm) \pm 0.1	Density (g/cm ³) \pm 0.2
J	Surface layer	1.7	3.35	6.83
	Film layer	216.8	0.004	7.96
	Interfacial layer	1.9	0.18	3.97
K	Surface layer	2.0	2.12	5.48
	Film layer	185.4	1.34	8.19
	Interfacial layer	5.5	0.70	2.41

F. Vibrational Sample Magnetometry

All the magnetic measurements were conducted at 300K by applying a magnetic field parallel to the film surface. Figure 49 and 50 show the hysteresis curves for samples A, B, C and D normalized to volume obtained using a vibrational sample magnetometer (VSM). The magnetic parameters extracted from these curves are shown in Table XV. All the samples show a saturation magnetization (M_s) value less than that of pure α -Fe reported in literature (1714 emu/cm³)²⁷. This decrease in saturation magnetization could be attributed to several factors including the presence of more than one phase in all these films as observed from the XRD patterns and the presence of a natively grown oxide layer as confirmed by XPS spectra. Samples A and B which show the presence of α' -Fe₁₆N₂ and/or α -Fe phase in their XRD patterns exhibit a higher M_s value as compared to samples C and D. This decrease in the M_s for samples C and D can be attributed to the presence of γ' -Fe₄N phase as reported in their XRD patterns (Figure 2).

The remanent magnetization (M_r) of samples A and B is 721 and 752 emu/cm³ respectively. As compared to the saturation magnetization for these samples, the remnant magnetization is low which affects the squareness of the hysteresis curves (Figure 50). The M_r approaches towards M_s for sample C (N₂ - 2.5 sccm). This significantly improves the squareness of the hysteresis curve. Further increasing the nitrogen flow rate to 5

sccm, the M_r slightly decreases as compared to the M_s value. Thus it can be suggested that the presence of the γ' - Fe_4N phase improves the squareness of the VSM curves.

It can also be observed from Figure 50 that the films fabricated at a nitrogen flow rate of 0.6 sccm (sample A) and 1.2 sccm (sample B) show a similar coercivity value. On increasing the nitrogen flow rate to 2.5 sccm and then to 5 sccm, a sharp decrease in coercivity is observed for samples C and D and they report a coercivity value of around. This decrease in the coercivity for samples C and D could be attributed to the presence of γ' - Fe_4N phase in the film which probably tends to reduce the magnetocrystalline anisotropy present in samples A and B due to strong (110) α -Fe and/or (220) α'' - Fe_{16}N_2 peaks.

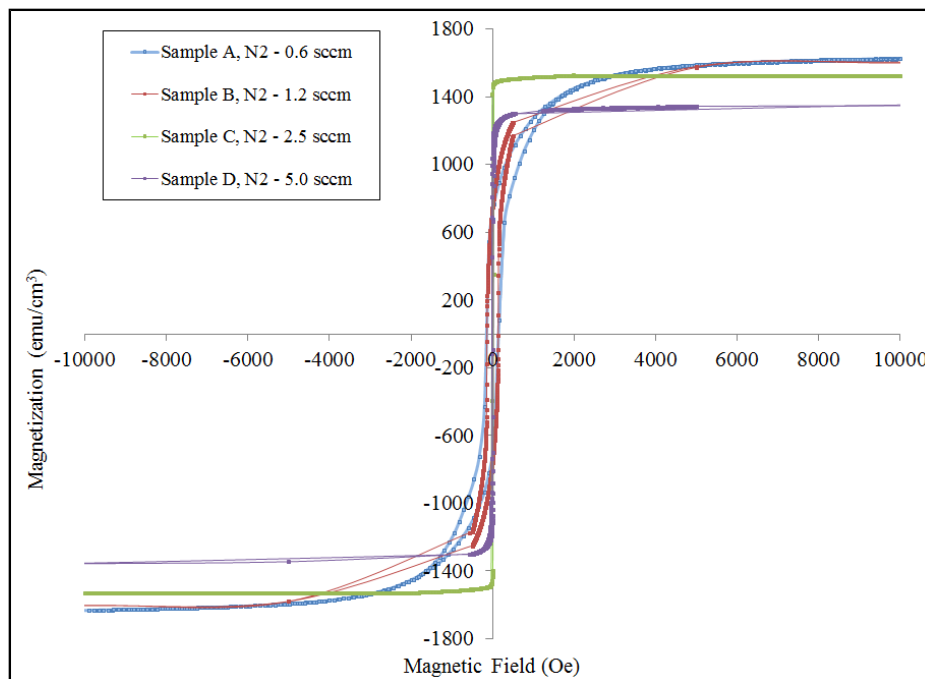


Figure 49. Hysteresis curves for samples A, B, C and D.

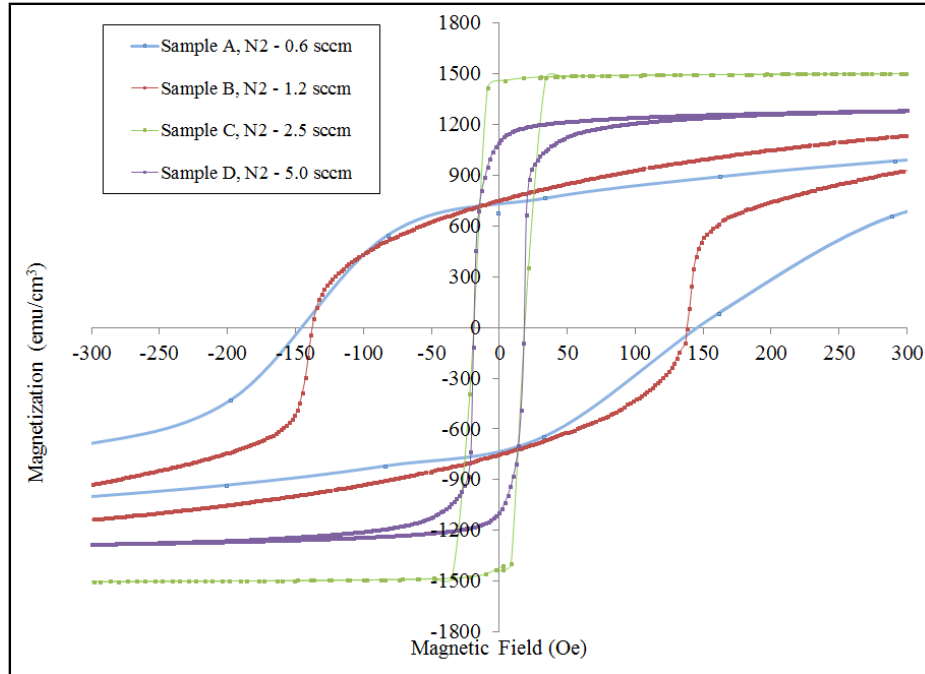


Figure 50. Expanded hysteresis curves for samples A, B, C and D.

Table XV. Magnetic parameters for samples A, B, C and D extracted from their VSM curves.

Sample	M_s (emu / cm ³) \pm 50	M_r (emu / cm ³) \pm 50	H_c (Oe) \pm 2.5
A	1650	721	148
B	1610	752	140
C	1520	1450	18.3
D	1360	1100	18.3

Figure 51 and 52 show the hysteresis curves for films fabricated by co-sputtering iron and copper at nitrogen flow rate of 5 sccm. Figure 53 and 54 show the hysteresis curves for films fabricated by co-sputtering iron and copper at nitrogen flow rate of 1.2 sccm respectively. The magnetic parameters extracted from these curves are tabulated in Table XVI and Table XVII respectively. All the co-sputtered films show a ferromagnetic behavior at 300°K. It can be observed that the M_s of samples E, F, G and H is lower than that of sample D and that of samples J and K is lower than that of sample B. This can be

attributed to the presence of copper which is nonmagnetic. The saturation magnetization decreases with an increasing copper sputtering power for both set of films (N_2 - 5 and 1.2 sccm). Previously conducted studies on copper incorporated iron nitrides ($Cu_xFe_{4-x}N$) suggests that the decrease in saturation magnetization is caused by copper atoms substituting the FCC crystal lattice²³. The presence of copper can also result in the formation of copper nitride (Cu_3N) which is a semiconductor and generally regarded as non-magnetic¹. In this work copper addition presumably formed γ' - $Cu_xFe_{4-x}N$ phase for samples E and F and G and Cu_3N phase for H as suggested by the XRD (Table III) and XPS peak positions for copper (Table IX) which contributed towards lowering the saturation magnetization of these films. For sample J, addition of copper led to the formation of $Fe_{0.5}Cu_{0.5}$ phase (Figure 4). Prior studies show that the saturation magnetization for $Fe_{0.5}Cu_{0.5}$ is lower than that of pure iron and decreases with increasing copper concentration⁴⁸. Thus a decrease in the saturation magnetization is observed for sample J. The saturation magnetization further decreases for sample K due to the presence of $\epsilon - Fe_3N$ phase which has the lowest saturation magnetization amongst iron nitride phases and $\zeta - Fe_2N$ which is a nonmagnetic phase. It can also be observed that the remanent magnetization for the two sets of co-sputtered films ($N_2 - 5$ and 1.2 sccm) decreased with increasing copper sputtering power.

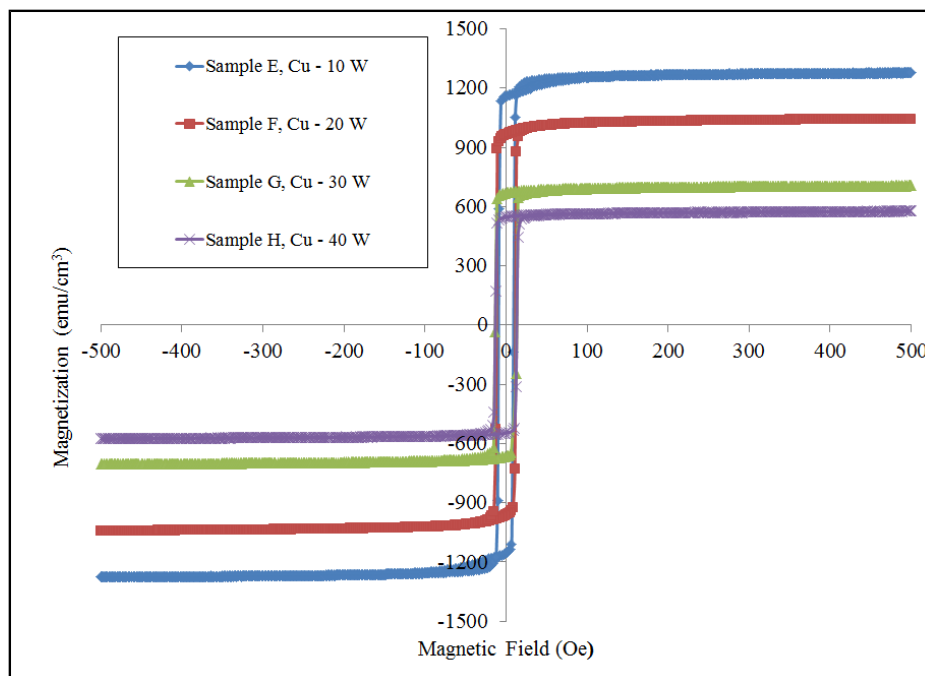


Figure 51. Hysteresis curve for samples E, F, G and H.

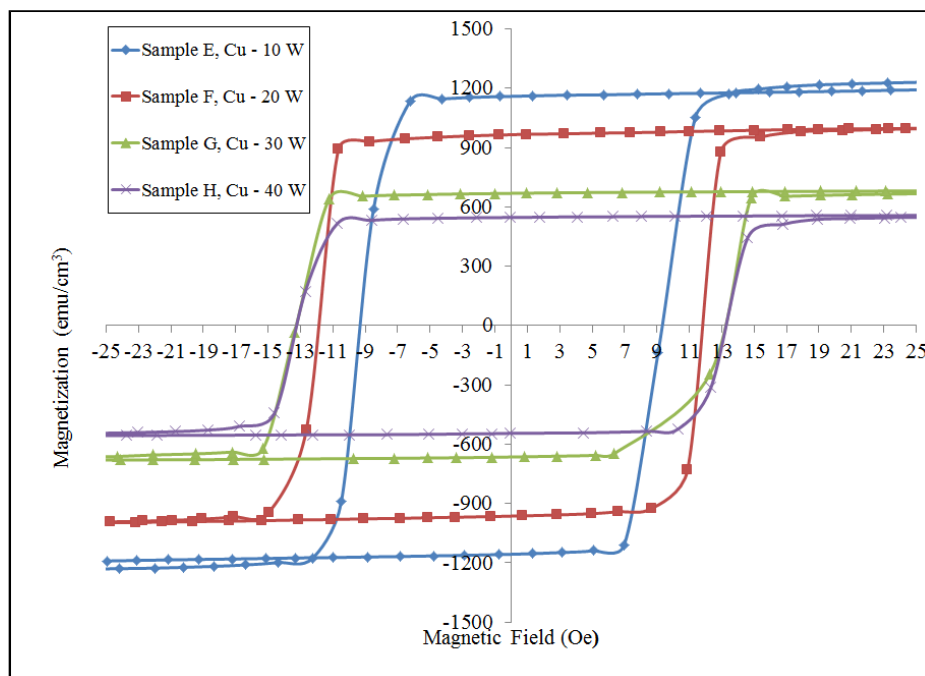


Figure 52. Expanded hysteresis curves for samples E, F, G and H.

Table XVI. Magnetic parameters for samples E, F, G and H extracted from the VSM curves.

Sample	M_s (emu / cm ³) \pm 50	M_r (emu / cm ³) \pm 50	H_c (Oe) \pm 2.5
E	1270	1160	9.2
F	1050	965	11.5
G	710	670	13.1
H	580	550	13.1

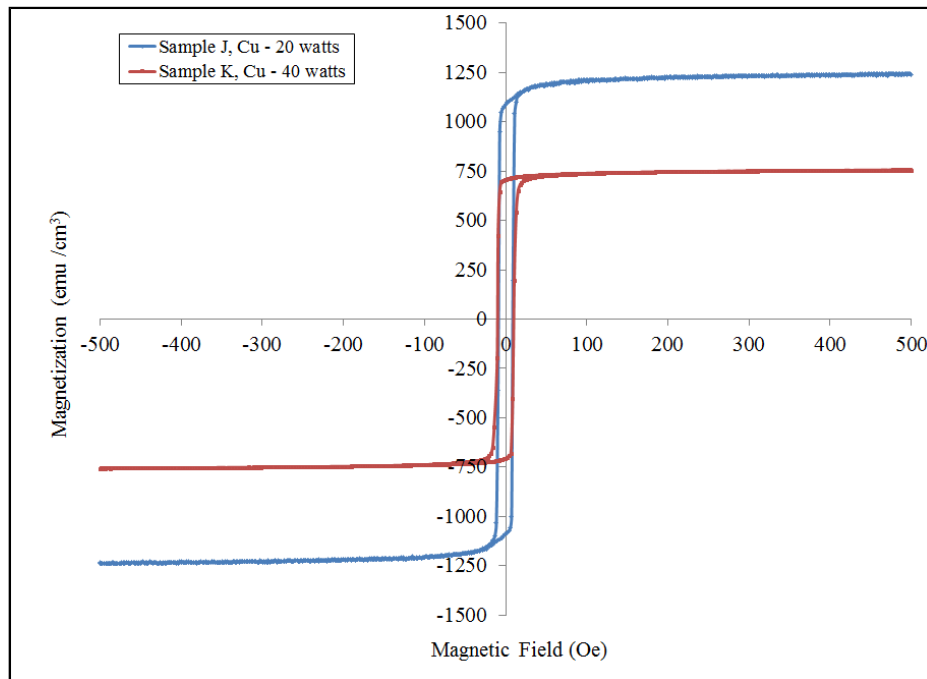


Figure 53. Hysteresis curves of samples J and K.

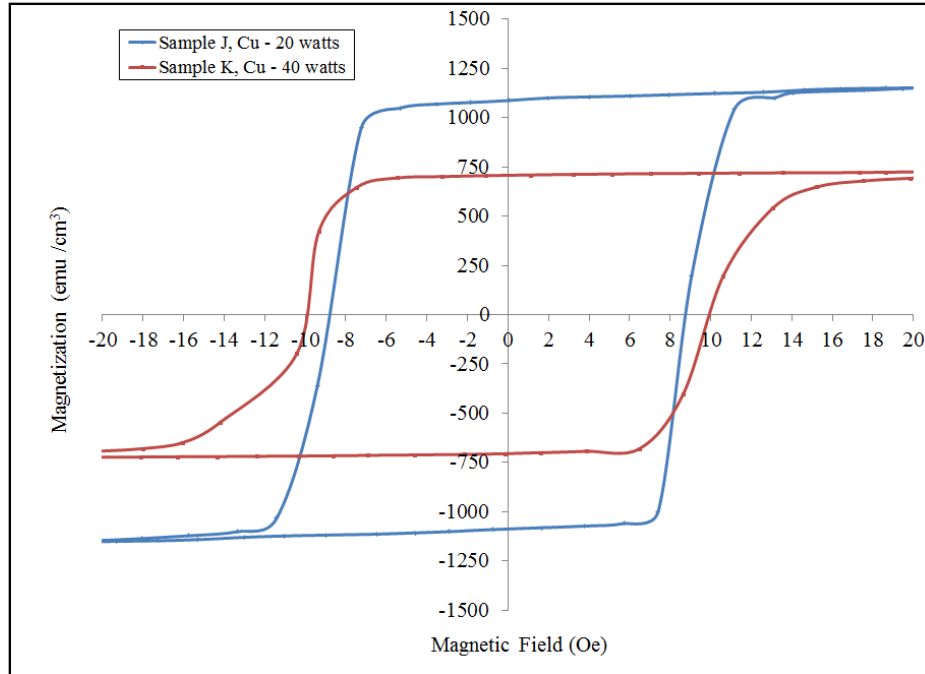


Figure 54. Expanded hysteresis curve for samples J and K.

Table XVII. Magnetic parameters for samples J and K extracted from the VSM curves.

Sample	M_s (emu / cm ³) \pm 50	M_r (emu / cm ³) \pm 50	H_c (Oe) \pm 2.5
J	1250	1095	8.8
K	750	705	10

The coercivity of a material is dependent on many factors including grain size and stress. Past literature suggests that the coercivity decreases on decreasing the grain size for nanometer size grains⁴⁹. From the SEM surface micrographs it appeared that the addition of copper led to a decrease in the grain size for the co-sputtered films as compared to their pure iron nitride counterparts fabricated at a the same nitrogen flow rates. Thus a corresponding decrease in the coercivity is consistent for the co-sputtered films fabricated at a nitrogen flow rate of 5 sccm (Table XVI) and 1.2 sccm (Table XVII) compared to their pure iron nitride counterparts (sample D and sample B, Table XV). It can also be qualitatively observed from Figure 52, that the coercivity increases slightly as the copper sputtering power is increased from 10 to 30 W and then remains the same for

the copper sputtering power of 40 W. Similarly for sample K (Cu - 40 W) a slight increase in coercivity is observed as compared to sample J (Figure 54).

IV. CONCLUSION

Thin films of iron nitride and iron-copper nitride were fabricated via reactive magnetron sputtering. XRD analysis revealed that increasing the nitrogen flow rate changed the phase formation in the iron nitride films. At lower nitrogen flow rates (0.6 sccm and 1.2 sccm) the films were found to be α'' -Fe₁₆N₂ and/or α -Fe dominant; and at higher nitrogen flow rates (2.5 and 5 sccm) they were found to be mixed phases of γ' – Fe₄N and α'' -Fe₁₆N₂ and/or α -Fe. The XRD analysis for iron-copper nitride films fabricated at a nitrogen flow rate of 5 sccm revealed the presence of γ' -Cu_xFe_{4-x}N phase where copper substitutes the corner and face-centered iron atoms in the FCC γ' -Fe₄N lattice. Also increasing the copper sputtering power led to a shift in the peak positions corresponding to the γ' -Cu_xFe_{4-x}N towards higher angles suggesting a decrease in the lattice parameters and/or strain in the lattice. The magnetic measurements confirmed that all the co-sputtered films record magnetic hysteresis loops. Copper tends to decrease the saturation magnetization in these films and thus increasing copper sputtering power results in a decrease in the M_s values. The coercivities of all the co-sputtered films has decreased as compared to their pure iron nitride counterparts. The remanent magnetization to the saturation magnetization for all the co-sputtered films is higher as compared to the pure iron nitride films. It can be concluded that copper addition to iron nitride thin films, results in films with soft magnetic properties and improved squareness of the hysteresis (M s H) loops. Thus these films could find a potential application in the magnetic data storage industries.

REFERENCES

1. D. Borsa, "Nitride-Based Insulating and Magnetic Thin Films and Multilayers"; PhD Thesis. University of Groningen, Netherlands, 2004.
2. J. W. Orton and C. T. Foxon, "Group III Nitride Semiconductors for Short Wavelength Light-Emitting Devices," *Rep. Prog. Phys.*, **61** [1] 1 (1998).
3. R. N. Panda and N. S. Gajbhiye, "Magnetic Properties of Nanocrystalline γ -Fe₄N and ϵ -Fe₃N Synthesized by Citrate Route," *IEEE Trans. Magn.*, **34** [2] 542-8 (1998).
4. C. L. Liu, P. K. Chu, G. Q. Lin, and M. Qi, "Anti-Corrosion Characteristics of Nitride-Coated Aisi 316l Stainless Steel Coronary Stents," *Surf. Coat. Technol.*, **201** [6] 2802-6 (2006).
5. S. N. Monteiro, A. L. D. Skury, M. G. de Azevedo, and G. S. Bobrovnitchii, "Cubic Boron Nitride Competing with Diamond as a Superhard Engineering Material – an Overview," *J. Mater. Res. Technol.*, **2** [1] 68-74 (2013).
6. S. Bhattacharyya, "Iron Nitride Family at Reduced Dimensions: A Review of Their Synthesis Protocols and Structural and Magnetic Properties," *J. Phys. Chem. C*, **119** [4] 1601-22 (2015).
7. N. Terada, Y. Hoshi, M. Naoe, and S. Yamanaka, "Synthesis of Iron-Nitride Films by Means of Ion Beam Deposition," *IEEE Trans. Magn.*, **20** [5] 1451-3 (1984).
8. S. Wang and M. H. Kryder, "Rf-Diode-Sputtered Iron Nitride Films for Thin-Film Recording Head Materials," *Journal of Applied Physics*, **67** [9] 5134 (1990).
9. Y. K. Kim and P. B. Narayan, "Magnetic, Microstructural, and Compositional Characterization of Fe–N Thin Films for Recording Sensor Applications," *J. Vac. Sci. Technol., A*, **13** [3] 1040-3 (1995).
10. T. K. Kim and M. Takahashi, "New Magnetic Material Having Ultrahigh Magnetic Moment," *Appl. Phys. Lett.*, **20** [12] 492-4 (1972).
11. D. Andriamandroso, L. Fefilatiev, G. Demazeau, L. Fournès, and M. Pouchard, "Mössbauer Resonance Studies on Sn Substituted Fe₄N," *Mater. Res. Bull.*, **19** [9] 1187-94 (1984).
12. B. Siberchicot, S. F. Matar, L. Fournes, G. Demazeau, and P. Hagenmuller, "Influence of the Substitution of Manganese for Iron in the Fe₄N Lattice on

- Particle Formation and Magnetic Properties," *J. Solid State Chem.*, **84** [1] 10-5 (1990).
13. S. K. Chen, S. Jin, T. H. Tiefel, Y. F. Hsieh, E. M. Gyorgy, and D. W. Johnson, "Magnetic Properties and Microstructure of Fe₄N and (Fe,Ni)₄N," *J. Appl. Phys.*, **70** [10] 6247-9 (1991).
 14. P. Mohn, K. Schwarz, S. Matar, and G. Demazeau, "Calculated Electronic and Magnetic Structure of the Nitrides NiFe₃N and PdFe₃N," *Phys. Rev. B*, **45** [8] 4000-7 (1992).
 15. D. Xue, F. Li, J. Yang, Y. Kong, and M. Gao, "Effects of Substitutional Atoms on the Properties of γ' -(Fe_{1-x}TM_x)₄N (TM = Co, Ni) Compounds," *J. Magn. Magn. Mater.*, **172** [1] 165-72 (1997).
 16. T. Xie, D.-S. Zheng, X.-H. Li, Y.-G. Ma, F.-L. Wei, and Z. Yang, "Study of Nanocrystalline Fe-Al-N Soft Magnetic Thin Films," *Chin. Phys.*, **11** [7] 725 (2002).
 17. J. Das, S. S. Kalarickal, K.-S. Kim, and C. E. Patton, "Magnetic Properties and Structural Implications for Nanocrystalline Fe-Ti-N Thin Films," *Phys. Rev. B*, **75** [9] 094435 (2007).
 18. P. P. Mishra, M. M. Raja, and R. N. Panda, "Enhancement of Magnetic Moment in Co Substituted Nanocrystalline ϵ -Co_xFe_{3-x}N (0.2 \leq x \leq 0.4) Synthesized by Modified Citrate Precursor Route," *Mater. Res. Bull.*, **75** 127-33 (2016).
 19. P. R. Ganz, G. Fischer, C. Sürgers, and D. M. Schaadt, "Cu-Doped Nitrides: Promising Candidates for a Nitride Based Spin-Aligner," *J. Cryst. Growth*, **323** [1] 355-8 (2011).
 20. D. M. Borsa, S. Grachev, and D. O. Boerma, "Development of Epitaxial Nitride-Based Bilayers for Magnetic Tunnel Junctions," *IEEE Trans. Magn.*, **38** [5] 2709-11 (2002).
 21. D. M. Borsa, S. Grachev, C. Presura, and D. O. Boerma, "Growth and Properties of Cu₃N Films and Cu₃N/ γ' -Fe₄N Bilayers," *Appl. Phys. Lett.*, **80** [10] 1823 (2002).
 22. C. Navío, J. Alvarez, M. J. Capitan, J. Camarero, and R. Miranda, "Thermal Stability of Cu and Fe Nitrides and Their Applications for Writing Locally Spin Valves," *Appl. Phys. Lett.*, **94** [26] 263112 (2009).
 23. R. S. de Figueiredo, J. Foct, A. V. dos Santos, and C. A. Kuhnen, "Crystallographic and Electronic Structure of Cu_xFe_{4-x}N," *J. Alloys Compd.*, **315** [1-2] 42-50 (2001).

24. K. H. Jack, "Binary and Ternary Interstitial Alloys. I. The Iron-Nitrogen System: The Structures of Fe₄N and Fe₂N," *Proc. R. Soc. A*, **195** [1040] 34-40 (1948).
25. K. Jack, "The Iron-Nitrogen System: The Crystal Structures of ϵ -Phase Iron Nitrides," *Acta Crystallogr.*, **5** [4] 404-11 (1952).
26. J. M. D. Coey and P. A. I. Smith, "Magnetic Nitrides," *J. Magn. Magn. Mater.*, **200** [1-3] 405-24 (1999).
27. B. D. Cullity and C. D. Graham, *Introduction to Magnetic Materials*; p. 544. Wiley-IEEE Press, 197 - 239 2008.
28. H. A. Wriedt, N. A. Gokcen, and R. H. Nafziger, "The Fe-N (Iron-Nitrogen) System," *Bull. Alloy Phase Diagrams*, **8** [4] 355-77 (1987).
29. K. H. Jack, "The Synthesis, Structure, and Characterization of α' -Fe₁₆N₂ (Invited)," *J. Appl. Phys.*, **76** [10] 6620-5 (1994).
30. D. C. Sun, C. Lin, and E. Y. Jiang, "Epitaxially Grown Fe₁₆N₂ Single-Crystal Films with High Saturation Magnetization Prepared by Facing Targets Sputtering," *J. Phys.: Condens. Matter*, **7** [18] 3667 (1995).
31. V. Hari Babu, J. Rajeswari, S. Venkatesh, and G. Markandeyulu, "Effect of Thickness on Structural and Magnetic Properties in Nanocrystalline Fe-N Thin Films," *J. Magn. Magn. Mater.*, **339** 1-5 (2013).
32. I. Dirba, M. B. Yazdi, A. Radetinac, P. Komissinskiy, S. Flege, O. Gutfleisch, and L. Alff, "Growth, Structure, and Magnetic Properties of Thin Films," *J. Magn. Magn. Mater.*, **379** 151-5 (2015).
33. Y. Na, C. Wang, J. Xiang, N. Ji, and J.-p. Wang, "Investigation of γ' -Fe₄N Thin Films Deposited on Si(1 0 0) and GaAs(1 0 0) Substrates by Facing Target Magnetron Sputtering," *J. Cryst. Growth*, **426** 117-22 (2015).
34. *Handbook of Deposition Technologies for Films and Coatings*, Second Edition ed. Edited by R. F. Bunshah. Noyes Publications, United States of America, 1994.
35. C. Lo, S. V. Krishnaswamy, L. N. Mulay, and R. A. Duffenbach, "Static Magnetic and Mössbauer Spectroscopic Measurements on Fe-N Thin Films," *J. Appl. Phys.*, **53** [3] 2745-7 (1982).
36. D. H. Mosca, P. H. Dionisio, W. H. Schreiner, I. J. R. Baumvol, and C. Achete, "Compositional and Magnetic Properties of Iron Nitride Thin Films," *J. Appl. Phys.*, **67** [12] 7514-9 (1990).

37. J. M. D. Coey and H. Sun, "Improved Magnetic Properties by Treatment of Iron-Based Rare Earth Intermetallic Compounds in Ammonia," *J. Magn. Magn. Mater.*, **87** [3] L251-L4 (1990).
38. K. H. J. Buschow, "New Developments in Hard Magnetic Materials," *Rep. Prog. Phys.*, **54** [9] 1123 (1991).
39. B. Ma, F. L. Wei, X. X. Liu, C. T. Xiao, and Z. Yang, "The Effect of Ta on Structure and Magnetic Properties in Fe–N Films," *Mater. Sci. Eng., B*, **57** [2] 97-101 (1999).
40. A. V. dos Santos and C. A. Kuhnen, "Electronic Structure and Magnetic Properties of CoFe₃N, CrFe₃N and TiFe₃N," *J. Alloys Compd.*, **321** [1] 60-6 (2001).
41. N. S. Gajbhiye, R. S. Ningthoujam, and S. Bhattacharyya, "Magnetic Properties of Co and Ni Substituted ϵ -Fe₃N Nanoparticles," *Hyperfine Interact.*, **164** [1] 17-26 (2005).
42. P. Mills and J. L. Sullivan, "A Study of the Core Level Electrons in Iron and Its Three Oxides by Means of X-Ray Photoelectron Spectroscopy," *J. Phys. D: Appl. Phys.*, **16** [5] 723 (1983).
43. W. Diekmann, G. Panzner, and H. J. Grabke, "The Bonding State of Nitrogen Segregated on Fe(100) and on Iron Nitrides Fe₄N and Fe₂N," *Surf. Sci.*, **218** [2] 507-18 (1989).
44. M. J. Rajman, S. V. Veprek and D. L. Cocke, "The Surface Properties and Reactivities of Plasma-Nitrided Iron and Their Relation to Corrosion Passivation," *J. Electrochem. Soc.*, **136** [12] 3655-62 (1989).
45. X. Wang, W. T. Zheng, H. W. Tian, S. S. Yu, and L. L. Wang, "Effect of Substrate Temperature and Bias Voltage on Dc Magnetron Sputtered Fe–N Thin Films," *J. Magn. Magn. Mater.*, **283** [2–3] 282-90 (2004).
46. A. P. Grosvenor, B. A. Kobe, M. C. Biesinger, and N. S. McIntyre, "Investigation of Multiplet Splitting of Fe 2p Xps Spectra and Bonding in Iron Compounds," *Surf. Interface Anal.*, **36** [12] 1564-74 (2004).
47. G. Soto, J. A. Díaz, and W. de la Cruz, "Copper Nitride Films Produced by Reactive Pulsed Laser Deposition," *Mater. Lett.*, **57** [26–27] 4130-3 (2003).
48. P. Crespo, M. J. Barro, I. Navarro, M. Vázquez, and A. Hernando, "Magnetic Properties of Fe_xCu_{1-x} Solid Solutions," *J. Magn. Magn. Mater.*, **140** 85-6 (1995).

49. N. Ma, X. Wang, W. T. Zheng, L. L. Wang, M. W. Wang, P. J. Cao, and X. C. Ma, "Influence of Si-N Interlayer on the Microstructure and Magnetic Properties of γ' -Fe₄N Films," *Appl. Surf. Sci.*, **254** [15] 4786-92 (2008).

APPENDIX

Focused Ion Beam (FIB) surface micrographs

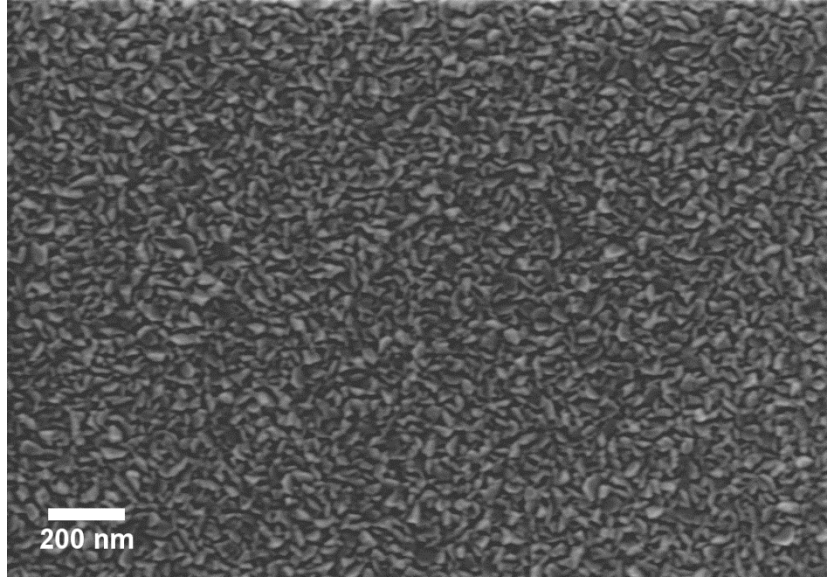


Figure 55. FIB micrograph of sample D fabricated at nitrogen flow rate of 5 sccm.

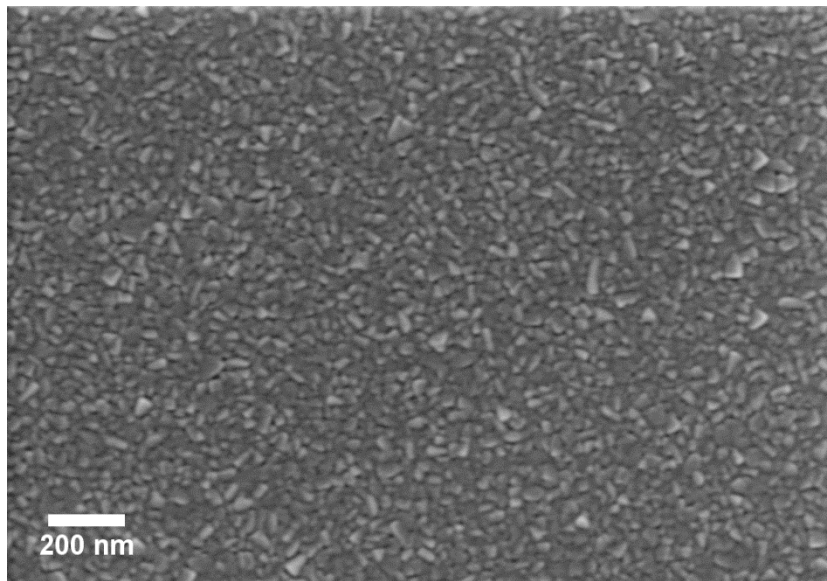


Figure 56. FIB micrograph of sample E fabricated at nitrogen flow rate of 5 sccm and a copper sputtering power of 10 W.

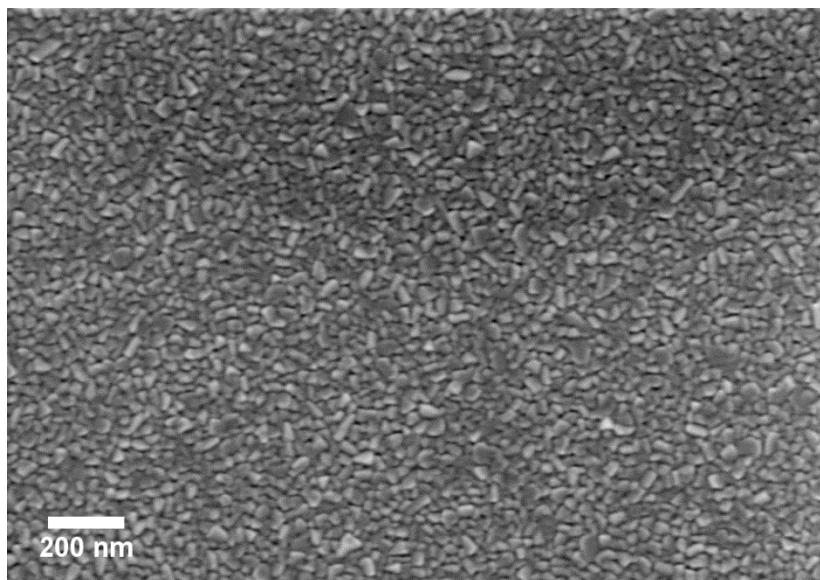


Figure 57. FIB micrograph of sample F fabricated at nitrogen flow rate of 5 sccm and a copper sputtering of 20 W.

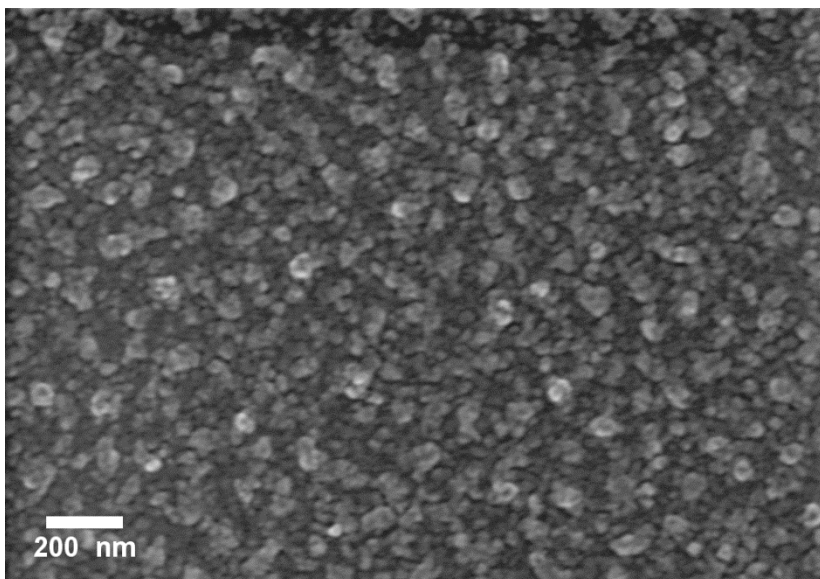


Figure 58. FIB micrograph of sample G fabricated at nitrogen flow rate of 5 sccm and a copper sputtering of 30 W.

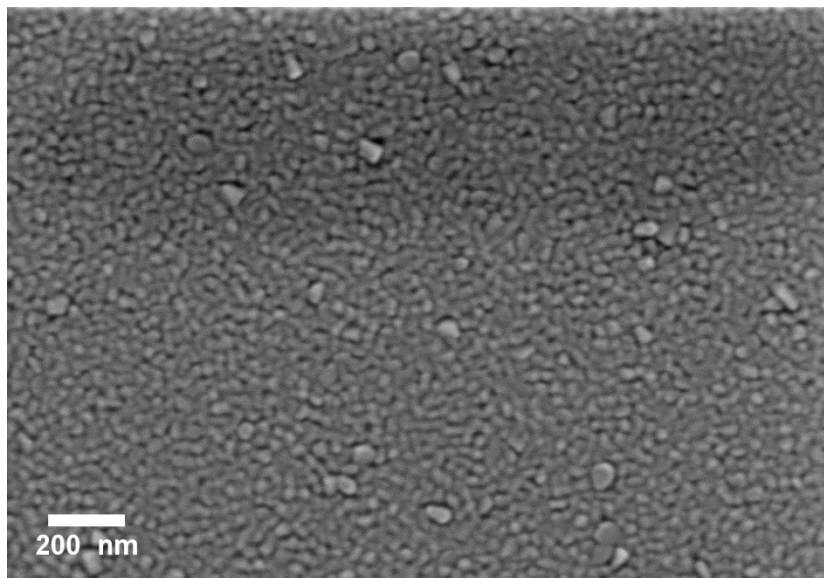


Figure 59. FIB micrograph of sample H fabricated at nitrogen flow rate of 5 sccm and a copper sputtering of 40 W.